

# AdaptNC: Adaptive Nonconformity Scores for Uncertainty-Aware Autonomous Systems in Dynamic Environments

Renukanandan Tumu<sup>1</sup> Aditya Singh<sup>1</sup> Rahul Mangharam<sup>1</sup>

## Abstract

Rigorous uncertainty quantification is essential for the safe deployment of autonomous systems in unconstrained environments. Conformal Prediction (CP) provides a distribution-free framework for this task, yet its standard formulations rely on exchangeability assumptions that are violated by the distribution shifts inherent in real-world robotics. Existing online CP methods maintain target coverage by adaptively scaling the conformal threshold, but typically employ a static nonconformity score function. We show that this fixed geometry leads to highly conservative, volume-inefficient prediction regions when environments undergo structural shifts. To address this, we propose **AdaptNC**, a framework for the joint online adaptation of both the nonconformity score parameters and the conformal threshold. AdaptNC leverages an adaptive reweighting scheme to optimize score functions, and introduces a replay buffer mechanism to mitigate the coverage instability that occurs during score transitions. We evaluate AdaptNC on diverse robotic benchmarks involving multi-agent policy changes, environmental changes and sensor degradation. Our results demonstrate that AdaptNC significantly reduces prediction region volume compared to state-of-the-art threshold-only baselines while maintaining target coverage levels.

## 1. Introduction

Autonomous systems operating in real-world environments face a constant challenge: distribution shift. These shifts, driven by changing environmental conditions, system degradation, or complex multi-agent interactions, can severely degrade the performance of predictive models. For safety-critical applications such as autonomous driving and robotic

navigation, identifying these shifts and providing robust, uncertainty-aware predictions is not just a performance requirement; it is a safety necessity (Lindemann et al., 2025; 2023; Yang et al., 2023; Tayal et al., 2025). Identifying this distribution shift and quantifying the uncertainty of predictors in these settings is a significant challenge. Conformal Prediction (CP) has emerged as a gold-standard framework for providing such reliability, offering distribution-free uncertainty quantification with formal coverage guarantees (Vovk et al., 2022). Although split conformal methods are widely used due to their simplicity and guarantees, they typically assume that the data distribution remains exchangeable with a held-out calibration set (Lei et al., 2018), an assumption which is violated under distribution shift.

Recent advances in Online Conformal Prediction have addressed this violation by adjusting the conformal quantile thresholds to maintain target coverage levels. This is commonly done through reweighting techniques (Tibshirani et al., 2019; Barber et al., 2023) or adaptive quantile adjustments (Gibbs & Candes, 2021; Gibbs & Candès, 2024; Zaffran et al., 2022). Although effective in achieving target coverage, these methods suffer from a critical limitation: they treat the nonconformity score function as fixed. The score function determines the geometry and efficiency of prediction regions. A static score function in a shifting environment often results in unnecessarily large conservative uncertainty bounds that lead to suboptimal control and decision-making. The choice and parameterization of these nonconformity scores significantly impact not only the efficiency (i.e., volume) of the prediction regions but also their informativeness for downstream decision-making tasks (Tumu et al., 2024).

In this paper, we propose **AdaptNC**, a novel framework that enables the *joint online adaptation* of both the conformal threshold and the nonconformity score parameters. Unlike existing methods that only tune the threshold, AdaptNC optimizes the underlying score function to ensure that prediction regions remain tight and informative even as the data distribution evolves. To handle non-stationarity, we introduce an *adaptive reweighting scheme* that leverages DtACI expert weights to prioritize the most relevant historical observations during score optimization. To mitigate

<sup>1</sup>Department of Electrical and Systems Engineering, University of Pennsylvania, Philadelphia, Pennsylvania. Correspondence to: Renukanandan Tumu <nandant@upenn.edu>.

“coverage shock” (the sudden instability in coverage that occurs when a score function is modified) we employ a counterfactual *replay mechanism* to recalibrate the quantile threshold following a score update.

**Contributions:** This paper addresses the challenge of constructing efficient, uncertainty-aware prediction regions under arbitrary distribution shift by contributing:

1. **Online Score Adaptation:** We present a method for the online optimization of nonconformity scores and their corresponding quantiles that minimizes prediction region volume while enabling adaptation to shifting distributions.
2. **Dynamic Weighting and Replay Buffer:** We develop a weighting mechanism for data based on distribution shift, and a replay mechanism to maintain coverage stability during score parameter transitions.
3. **Empirical Validation on Robotic Benchmarks:** We evaluate AdaptNC on robotic tasks involving structural shifts, including multi-agent policy changes and sensor degradation. We demonstrate that AdaptNC significantly reduces prediction volume compared to state-of-the-art online CP baselines while rigorously maintaining target coverage levels.

## 2. Problem Setup and Preliminaries

### 2.1. Online Regression Setting

We consider an online regression setting where, at each time step  $t = 1, 2, \dots, T$ , the learner observes a feature vector  $X_t \in \mathcal{X}$ , produces a point prediction  $\hat{Y}_t = \{\hat{y}_{t+1}, \dots, \hat{y}_{t+\tau}\} \in \mathcal{Y}^\tau$  for outcomes over  $\tau$  steps, and subsequently observes the true outcome  $Y_t \in \mathcal{Y}^\tau$ . A predictor  $h : \mathcal{X} \rightarrow \mathcal{Y}^\tau$  is used to generate the point predictions, i.e.,  $\hat{Y}_t = h(X_t)$ . The joint distribution of  $(X_t, Y_t)$  may change over time, reflecting distribution shift.

We seek to build a set where the true outcome  $Y_t$  is above this set with probability  $\alpha$ . This is known as the miscoverage rate, with  $\delta = 1 - \alpha$  being the coverage rate. The sets are known as prediction regions  $\mathcal{C}_t(X_t; \theta_t, q_{\delta, \mathcal{D}_t}) \subseteq \mathcal{Y}^\tau$  for each time  $t$  with a target miscoverage rate of  $\alpha$  (equivalently, coverage rate  $1 - \alpha$ ). The variable  $q_{\delta, \mathcal{D}_t}$  is the  $\delta$  quantile of the dataset  $\mathcal{D}_t$ . The prediction regions are constructed using a non-conformity score function  $s(X_t, y; \theta_t)$  where  $\theta_t$  are learnable parameters updated online. Specifically, the prediction region is defined as:  $\mathcal{C}_t(X_t; \theta_t, q_{\delta, \mathcal{D}_t}) := \{y \in \mathcal{Y}^\tau : s(X_t, y; \theta_t) \leq q_{\delta, \mathcal{D}_t}\}$ .

### 2.2. Desiderata

We pursue two main objectives in this online regression setting, coverage and efficiency, under distribution shift.

**Coverage.** Due to distribution shift, we do not expect to meet this coverage target at all times. Instead, we seek the asymptotic property that our long-run miscoverage rate approaches  $\alpha$ , under the assumption that the distribution stabilizes after a period of shift. We define the error indicator  $\mathbf{err}_t = \mathbb{1}\{Y_t \notin \mathcal{C}_t(X_t; \theta_t, q_{\delta, \mathcal{D}_t})\}$ , and state our desired coverage property as follows:

$$\lim_{T \rightarrow \infty} \frac{1}{T} \sum_{t=1}^T \mathbf{err}_t = \alpha. \quad (1)$$

**Efficiency** We would also like to ensure that the prediction regions  $\mathcal{C}_t$  are small and informative to downstream algorithms. Thus, while maintaining the coverage guarantee above, our objective is to minimize the volume of the prediction set  $\mathcal{C}_t$ . We formulate the optimization problem:

$$\min_{\theta_t} \text{Vol}(\mathcal{C}_t(X_{t+1}; \theta_t, q_{\delta, \mathcal{D}_t})) \quad (2a)$$

$$\text{s.t. } \Pr[Y_{t+1} \in \mathcal{C}_t(X_{t+1}; \theta_t, q_{\delta, \mathcal{D}_t})] \geq 1 - \alpha. \quad (2b)$$

### 2.3. Preliminaries

**Conformal Prediction.** Conformal prediction (CP) provides distribution-free, finite-sample prediction regions which guarantee marginal coverage with high probability under the assumption of exchangeable data (Vovk et al., 2022; Lei et al., 2018). Split conformal prediction and its variants, like jackknife+ (Lei et al., 2018; Barber et al., 2020), extend this framework to modern machine learning train-test paradigms while reducing the computational cost of full conformal methods. Much of this literature treats the non-conformity score as fixed, with scores resembling residuals or norms for regression tasks, and focuses on how to calibrate the conformal quantile to ensure coverage. Our work targets the non-conformity score itself, in order to provide efficient and adaptive prediction regions. The guarantee that Conformal Prediction seeks to provide is marginal coverage, i.e.,  $P(Y_t \in \mathcal{C}_t(X_t; \theta_t, q_{\delta, \mathcal{D}_t})) \geq 1 - \alpha$ . This guarantee holds in finite samples under exchangeability, but is not guaranteed to work under distribution shift.

**Maintaining Coverage under Distribution Shift.** In settings where distribution shift is present, the exchangeability assumption is violated, and conformal prediction methods may fail to maintain coverage. Our method builds on recent work that extends conformal prediction to settings with distribution shift by adapting the calibration quantile online. DtACI maintains coverage under arbitrary distribution shifts by adaptively reweighting a set of candidate adaptation rates based on their historical performance. It obtains a long-term coverage guarantee of the form in Equation (1) in settings where the size of the distribution shift decays over time.

The DtACI algorithm seeks to compensate for distribution shift by changing the conformal quantiles  $\alpha_t$  used to select

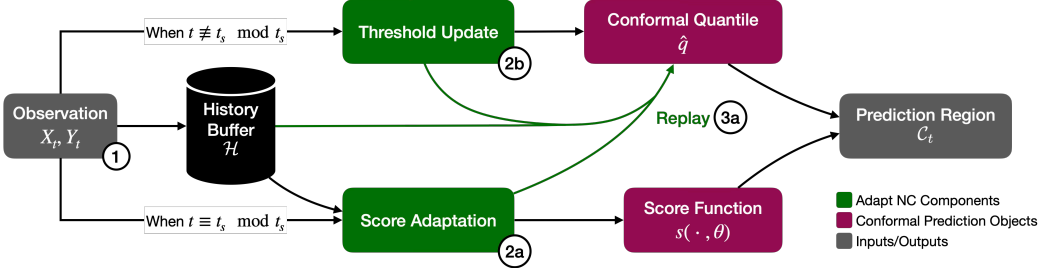


Figure 1. The AdaptNC framework is an online algorithm designed to handle distribution shifts. The above figure shows the procedure at a timestep  $t$ . (1) The observation for the current timestep arrives, and is added to the history buffer. Every  $t_s$  timesteps, the **score function** is adapted by **weighted score adaptation** (2a). This adaptation yields a score function  $s(\cdot, \theta_t)$ , the **replay** algorithm (3a) compensates for the distribution shift generated by the change in score function by replaying recent samples from the history buffer  $\mathcal{H}$  and generates the conformal quantile  $\hat{q}$ . When the score is not being adapted, only the **conformal quantile** is adapted through the **threshold update** step.

the score threshold  $q_{1-\alpha, t}$ . The algorithm aims to minimize the difference between the optimal quantile  $\alpha_t^*$  that would yield exact coverage at time  $t$  and the estimated quantile  $\alpha_t$ . This difference is bounded in Theorem C.1. Observations in the DtACI algorithm are quantiles  $\beta_t$ , which are the lowest empirical quantiles of the dataset  $\mathcal{D}_t$  that would have covered the true outcome at time  $t$ . Formally,

$$\beta_t := \sup \{ \beta : Y_t \in \{y : s(X_t, y; \theta_t) \leq \hat{q}_{\beta, \mathcal{D}_t}\} \} \quad (3)$$

DtACI maintains a set of  $k$  candidate adaptation rates  $\{\gamma_i\}_{i=1}^k$  and corresponding weights  $\{w_{k,t}\}_{k=1}^K$ . At each time step, the algorithm performs an exponential weights update on the weights based on the error incurred by each candidate rate. An averaged quantile  $\bar{\alpha}_t$  is then computed using the weights, and the quantile threshold  $q_{1-\bar{\alpha}_t, \mathcal{D}_t}$  is updated accordingly. The algorithm is presented in Algorithm 3 (in Appendix B).

### 3. Related Work

Conformal prediction regions are used for applications in safety-critical systems, such as autonomous driving (Lindemann et al., 2023; Dixit et al., 2023), where it is crucial to maintain valid uncertainty estimates despite changing conditions. Efficient and adaptive conformal prediction methods can enhance the reliability of these systems by providing tighter uncertainty bounds that reflect the current data distribution. Dixit et al. (2023) demonstrate the utility of adaptive conformal prediction in autonomous driving scenarios, providing a framework for utilizing adaptive conformal methods in control. The ability to generate efficient prediction regions for control has been the subject of previous work, as the reduction in the volume of prediction regions directly impacts the conservativeness of control strategies (Lindemann et al., 2023; Tumu et al., 2024). However, these methods design static nonconformity scores without adaptation to distribution shifts, potentially leading to suboptimal performance in dynamic environments.

**Conformal Prediction under Distribution Shift.** Two primary approaches have been proposed to extend confor-

mal prediction to settings with distribution shift. The first approach is to modify the calibration set to better reflect the test distribution. This can be done by reweighting calibration points based on their similarity to the test point (Barber et al., 2023; Tibshirani et al., 2019). These methods have been applied to multi-agent settings by Kuipers et al. (2024) and Binny & Dixit (2025).

The second approach is to adapt the quantile used for calibration over time, as in Adaptive Conformal Inference (ACI) (Gibbs & Candes, 2021) and other approaches like Multi-valid Conformal Prediction (Bastani et al., 2022) and AgACI (Zaffran et al., 2022). These methods adjust the quantile based on recent coverage performance, allowing them to maintain coverage under certain types of distribution shift. DtACI allows for subsequent scores to be generated using different non-conformity scores, making it a natural fit for our framework.

**Efficient Non-Conformity Scores.** The design of volume-efficient non-conformity scores has been the focus of recent work in conformal prediction for various environments (Kiyani et al., 2024; Gao et al., 2025), including control and robotics settings multi-dimensional outputs (Tumu et al., 2024; 2023; Cleaveland et al., 2024; Braun et al., 2025). Our approach extends this line of work by adapting the non-conformity score online to maintain efficiency under distribution shift.

### 4. AdaptNC Method

Our method, Adaptation of Non-Conformity scores (AdaptNC) is designed to maintain efficient and valid conformal prediction regions in settings with distribution shift. AdaptNC has three steps (1) **Conformal Threshold Update** (2) **Score Parameter Adaptation**, and (3) **Replay**. In the threshold update step, we choose the conformal quantile  $q_{1-\bar{\alpha}_t, \mathcal{D}_t}$  corresponding to the current score function parameters. In the score parameter adaptation step, we use the current estimates of the rate of change of the data distribution to fit efficient non-conformity score parameters  $\theta_t$

to the data. Finally, in the replay step, we account for the change in the distribution of the score functions by replaying recent observations, in order mitigating abrupt shifts in coverage. Due to computational intensity, steps (2) and (3) are only run every  $t_s$  timesteps. The AdaptNC algorithm is presented pictorially in Figure 1, and in detail in Algorithm 2 (in Appendix B).

**Conformal Threshold Update** The aim of this step is to approximate the true conformal quantile  $\alpha_t^*$ , which is the quantile of the data such that  $\Pr[Y_{t+1} \in \mathcal{C}_t(X_{t+1}; \theta_t, q_{\alpha_t^*, \mathcal{D}_t})] \geq 1 - \alpha$ . The conformal threshold update step uses the framework of the DtACI algorithm (Algorithm 3) to update its estimate of the true conformal quantile  $\alpha_t$  based on the observed scores. To enable coverage under unknown distribution shift,  $k$  ACI (Gibbs & Candes, 2021) experts are maintained and dynamically reweighted. The procedure involves calculating an inverse quantile to transform the raw non-conformity score, expert reweighting, and finally expert update.

First, we save tuples  $(X_t, Y_t, \hat{Y}_t)$  in a history buffer  $\mathcal{H}$ . For each observation,  $\beta_t$  is calculated according to Equation (3). The dataset  $\mathcal{D}_t$  used in the quantile calculation is a rolling window of the last  $W$  timesteps. Based on the error between the predicted quantile for each expert  $\alpha_t^i$  and the observed  $\beta_t$ , the weight  $w_t^i$  is exponentially reweighted. When these weights are applied to the experts, we get the algorithm's estimate of the current conformal quantile  $\bar{\alpha}_t$ . Finally, each expert is updated according to the expert learning rate  $\gamma_i$  and the error indicator  $\text{err}_t^i$ , which is 1 if the observation is not covered by the  $i$ -th expert, and 0 otherwise. The complete DtACI algorithm is presented in Algorithm 3 (in Appendix B).

**Score Parameter Adaptation** The objective of this step is to find the parameters  $\theta_t$  to best achieve the efficiency goal in Equation (2). This problem is challenging because we do not know what the distribution will be in future timesteps. Fortunately, the expert weights  $w_t^i$  and their expert learning rates  $\gamma_i$  provide an estimate of how quickly the distribution is changing. In this step, we reweight the data in our history buffer and formulate an optimization problem to minimize the volume with respect to the current estimate of the data distribution.

First, we perform a reweighting of the data in the history buffer  $\mathcal{H}$  based on our estimate of distribution shift. This estimate takes the form of the expert learning rates and weights  $\gamma_t, w_t^i$ . Adaptive reweighting is important because it allows for the algorithm to “forget” past data based on the rates of change of the distribution when the distribution changes quickly, and utilize it for better estimates when the distribution is stable. For each historical timepoint, the weight  $\omega_t$  is assigned based on Equation (4), inducing the

distribution  $\mathcal{H}_t^\omega$ .

$$\bar{\omega}_t = \sum_{i=1}^k w_t^i (1 - \gamma_i)^{T-t+1}, \quad \omega_t = \bar{\omega}_t / \sum_{j=1}^{|\mathcal{H}|} \bar{\omega}_j. \quad (4)$$

Using this reweighted distribution, we can formulate the optimization problem below

$$\min_{\theta_t} \text{Volume}(\{y : s(X_t, y; \theta_t) \leq q_{1-\alpha, t}\}) \quad (5a)$$

$$\text{s.t. } \mathbb{P}_{(X_t, Y_t) \sim \mathcal{H}_t^\omega}(Y_t \in \hat{\mathcal{C}}_t(X_t; \theta_t, \mathcal{D}_t)) \geq 1 - \alpha \quad (5b)$$

This optimization problem seeks to minimize the volume of the set covering  $1 - \alpha$  of the weight of the reweighted data distribution  $\mathcal{H}_t^\omega$ . This optimization can be performed using gradient-based methods or other suitable optimization techniques. In our approach, we use a variant of the method proposed in Tumu et al. (2024) to optimize the score parameters, while yielding convex shapes which are easy to use in downstream applications (Lindqvist et al., 2020). In this variant, we introduce a Monte-Carlo density estimation technique that avoids the computational complexity challenges in Tumu et al. (2024), and eliminate the clustering algorithm for simplicity.

This procedure takes place in two steps: (1) density estimation and (2) shape template optimization. Density estimation aims to identify the highest density regions of the reweighted data points in  $\mathcal{H}$ . Shape template optimization then fits convex shapes to cover these high-density regions, which are used to define the non-conformity score.

To identify the high-density region, we use the weighted sample points from our history buffer  $\mathcal{H}$  to construct a Kernel Density Estimate (KDE) (Parzen, 1962). We identify the highest density regions that cover a proportion  $1 - \alpha$  of the total density mass through sampling a large number of points from the KDE and identifying their likelihoods. We select the top  $1 - \alpha$  proportion of these sampled points based on their likelihoods to form our set of high-density points  $\mathcal{D}$ . This yields a set of points  $\hat{R}_t$  which comprise the high-density region. The complete algorithm is presented in Section B.4, along with a proof of asymptotic convergence.

Armed with our high-density region  $\hat{R}_t$ , we fit a convex hull shape template to cover these points. The parameters of this shape template are  $\theta_t = \{A \in \mathbb{R}^{r \times p}, b \in \mathbb{R}^r\}$ , where  $r$  is the number of facets of the hull. The non-conformity score is then defined based on the distance of a point  $y$  from the convex hull defined by these shape templates:

$$s(X_t, y; \theta_t) = \max_{j \in 1, \dots, p} A_j(y - h(X_t)) - b_j \quad (6)$$

We identify this convex hull of the points in  $\hat{R}_t$  using the QuickHull algorithm (Barber et al., 1996).

**Replay** While we could directly use this score function in the threshold update step, as the underlying DtACI algorithm allows for changes in the score function, we pay an insidious penalty for this. This penalty is expressed in the regret guarantee Theorem C.1, where the error is bounded by a term proportional to the square root of the difference between the true  $\alpha^*$  in consecutive time steps. While this is normally small, changing the non-conformity score function parameters can result in a very large jump in the  $\alpha^*$ . Theoretical and empirical evidence for the necessity of the replay methodology is presented in Section 5.2 and Figure 2.

In order to mitigate this difference, we replay the past  $W$  data points with a freshly initialized set of expert weights and the new score function parameters  $\theta_t$ . This can be interpreted as a counterfactual evaluation of the conformal threshold update, where we identify the the value of  $\alpha_t$  under the assumption that previous observations were scored under the parameters  $\theta_t$  as opposed to other score parameters. Due to the exponential weight updates, the estimate of  $\alpha_{t+1}$  is tied to the estimate of  $\alpha_t$ , which may have been made using a  $\beta_t$  that is much different to the current one by virtue a change in the score parameter. The counterfactual Replay mitigates this problem by resetting the  $\alpha_t$  update chain and evaluating past data through the lens of the new score parameters.

## 5. Theoretical Analysis

We will show that our method preserves the theoretical guarantees of DtACI, namely the regret and long-term coverage guarantees. We will build on this theory, and show that the score adaptation procedure we propose will also stabilize in the same setting as the long-term coverage guarantee. Finally, we will show a decomposition of distribution shift into the data-driven and score function driven parts, and provide evidence that this shift is observed in practice.

### 5.1. Coverage Guarantees

Our use of DtACI provides a regret guarantee for the adaptive miscoverage level selection procedure. The following remark is adapted from Gibbs & Candès (2024), and presented in full in Theorem C.1.

The Remark 5.2 states that the regret of our adaptive miscoverage level selection procedure is bounded by two terms: a term that decreases with increases in the size of the window  $|W|$ , and a term that depends on the total variation in the optimal miscoverage levels  $\alpha_t^*$  over the window. This means that if the optimal miscoverage levels do not change too much over time, our procedure will perform nearly as well as if we had known the optimal levels in advance.

**Assumption 5.1.** Let  $\gamma_{max} := \max_{1 \leq i \leq k} \gamma_t$  and assume that  $\gamma_1 < \gamma_2 < \dots < \gamma_k$  where  $\gamma_{i+1}/\gamma_i \leq 2$  for all  $1 < i \leq k$ , and that  $\ell(\beta_t, \theta) := \alpha(\beta_t - \theta) - \min\{0, \beta_t - \theta\}$

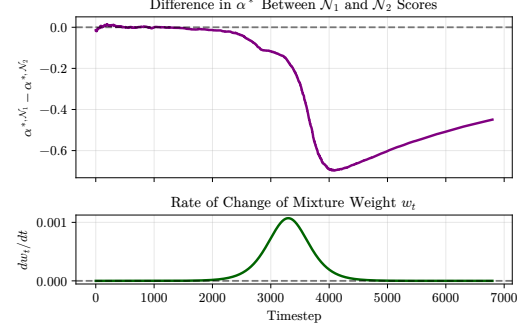


Figure 2. This figure shows the change in the optimal threshold  $\alpha_t^*$  based on scores from the initial and final distributions,  $\mathcal{N}_1$  and  $\mathcal{N}_2$ . The bottom pane shows the rate of distribution change, while the top shows the difference between optimal quantiles.

**Remark 5.2.** Then, for any window  $W = [r, s] \in [T]$  and any sequence  $\alpha_r^*, \dots, \alpha_s^* \in [0, 1]$ , and  $\eta = \sqrt{\frac{\log(2k|W|) + 1}{\sum_{t=r}^s \mathbb{E}[\ell(\beta_t, \alpha_t)^2]}}$  and  $\sigma = 1/(2|W|)$ ,

$$\frac{1}{|W|} \sum_{t=r}^s \ell((\beta_t, \bar{\alpha}_t)) - \frac{1}{|W|} \sum_{t=r}^s \ell((\beta_t, \alpha_t^*)) \leq O\left(\frac{\log(|W|)}{|W|}\right) + O\left(\sqrt{\frac{\sum_{t=r+1}^s |\alpha_t^* - \alpha_{t-1}^*|}{|W|}}\right). \quad (7)$$

The DtACI procedure has a randomized variant which provides the guarantee of long-term coverage (Gibbs & Candès, 2024, Theorem 6) approaching the target level Equation (1). This theorem is presented in Theorem C.2, and it assumes that in a setting when the distribution stabilizes, we can send  $\sigma, \eta \rightarrow 0$  over time. We show that under these same conditions, the non-conformity score function will also stabilize. The proof of the theorem is in Appendix Section C.3.

**Theorem 5.3** (Score Function Stability). *Consider the same modified version of Algorithm 3 as in Theorem C.2. Let  $\lim_{t \rightarrow \infty} \eta_t = \sigma_t = 0$ , and the number of data samples and Monte Carlo samples in Algorithm 4  $N, M \rightarrow \infty$ . Then the non-conformity score functions will stabilize:  $s(\cdot; \theta_t) = s(\cdot; \theta_{t+1})$  as  $t \rightarrow \infty$ .*

### 5.2. Replay

While changing the score function maintains the regret guarantee in Theorem C.1, the changes can have an outsize impact on the regret by virtue of producing changes in  $\alpha^*$ . The counterfactual replay mechanism proposed in Section 4 aims to mitigate this issue. In this section, we provide an intuitive explanation and empirical evidence in support.

**Proposition 5.4.** *Let  $\mathcal{D}_t$  and  $\mathcal{D}_{t+1}$  be the joint distributions of inputs and observations  $(X_t, Y_t)$  at times  $t$  and  $t+1$ . Assume that the total variation distance ( $\mathbf{TV}$ ) between the two distributions is bounded  $\mathbf{TV}(\mathcal{D}_t, \mathcal{D}_{t+1}) \leq \delta$ . For a*

fixed score function  $s(\cdot)$ , and a fixed score parameter  $\theta$  let  $S_{\theta,t}$  be the random variable  $s(X, Y, \theta)$  where  $(X, Y) \sim \mathcal{D}_t$ , and  $S_{\theta,t+1}$  be the random variable where  $(X, Y) \sim \mathcal{D}_{t+1}$ . Then, the **TV** distance between the score distributions will be less than  $\delta$ :  $\mathbf{TV}(S_{\theta,t}, S_{\theta,t+1}) \leq \delta$

*Proof.* This follows from the Data Processing Inequality (Polyanskiy & Wu, 2025, Theorem 7.4) with score function  $s(\cdot; \theta)$  as channel, and  $f$ -divergence as **TV** distance.  $\square$

**Remark 5.5.** The score distribution is a function of the underlying data and the score function used to process it. Assuming the shift in  $\theta$  we can decompose the distribution shift as follows due to Proposition 5.4.

$$\mathbf{TV}(S_{\theta_t,t}, S_{\theta_{t+1},t+1}) \leq \delta + \mathbf{TV}(S_{\theta_t,t+1}, S_{\theta_{t+1},t+1}) \quad (8)$$

We are concerned mainly with the change that this distribution shift induces in the optimal  $\alpha^*$ . While we do not have theory for this, we provide experimental evidence in a controlled setting, where data is drawn from a mixture of two Gaussians  $\mathcal{N}_1$  and  $\mathcal{N}_2$ , mixed by a changing weight  $w_t$ , we calculate the optimal  $\alpha_t^*$  where the score function is the negative log-likelihood for each distribution. We can see in Figure 2 that the distribution shift induces large changes in  $\alpha^*$ , which would induce large regret in the score update procedure. The theoretical maximum difference is 1, and the maximum observed difference was  $-0.7$ . Further details about this experiment are provided in Appendix D.1.

## 6. Experiments

Our objective is to demonstrate that jointly adapting the nonconformity score and its threshold enables tight uncertainty regions under distribution shift while preserving user-specified coverage. We evaluate this using **global coverage**, defined as  $1 - \frac{1}{T} \sum_{t=0}^T \mathbf{err}_t$ , which measures recovery of the target coverage level, and the **average coverage volume per covered timestep**, which quantifies conservatism. To assess temporal behavior, we report a **local coverage** metric, defined by  $1 - \frac{1}{w} \sum_{t=\frac{w}{2}+1}^{t+\frac{w}{2}} \mathbf{err}_t$ , a sliding-window average of size  $w$  which is particularly informative under distribution shifts.

**Baselines.** We evaluate the proposed method against three baselines. **(1) DtACI:** DtACI adapts coverage over time by adjusting the prediction threshold but employs a fixed nonconformity score. Comparing against DtACI isolates the effect of score-function adaptation and enables the assessment of AdaptNC’s ability to recover tighter uncertainty regions under distribution shift. **(2) Split Conformal Prediction:** Standard split conformal prediction relies on the exchangeability assumption and does not account for distribution shifts. Comparison with this baseline highlights the importance of adaptivity in settings with distribution shift. **(3) AdaptNC without Replay:** As an ablation, we consider

AdaptNC without Replay to examine the role of replay in stabilizing adaptation and mitigating coverage shock.

### 6.1. Indoor Localization under Multipath Fading

In this case study, we evaluate the performance of AdaptNC in a setting with environmental shift. The case study examines an indoor localization scenario, where a robot continuously estimates its planar position using received signal strength indicator (RSSI) measurements from a small number of fixed WiFi routers. The robot operates in a bounded two-dimensional indoor environment with 4 routers at known locations and follows double-integrator dynamics while executing random bounded motions. RSSI measurements are generated using a standard log-distance path-loss model with temporally correlated shadowing (Gudmundson, 1991) and small-scale fading (Jakes & Cox, 1994; Rappaport, 2010), capturing realistic wireless channel variability. Localization is performed using a fixed, model-based predictor that inverts RSSI measurements to distance estimates and combines iterative least-squares position estimation with an  $\alpha$ - $\beta$  tracking filter. Importantly, the predictor neglects shadowing and fading effects and is tuned only under nominal conditions, with no learning or online adaptation at test time. As a result, a distribution shift emerges from the persistent temporal evolution of the wireless channel, which is not captured by the predictor’s underlying assumptions. Evaluation is conducted over a single rollout of 6000 time steps without resets, during which this mismatch accumulates over time, yielding a realistic and challenging benchmark for adaptive uncertainty quantification. Full simulation details are provided in Appendix D.2.

**Performance Evaluation and Comparative Analysis:** As shown in Table 1, AdaptNC achieves a global coverage of 90.65%, which is closest to the target level of 90% among all methods, while attaining the smallest volume per covered timestep. In contrast, DtACI and Split Conformal Prediction exhibit overcoverage with substantially larger uncertainty volumes, corresponding to 130% and 326% of AdaptNC’s volume, respectively, reflecting their limited ability to adapt to distribution shift. AdaptNC without replay similarly exhibits overcoverage and larger uncertainty regions, with volumes reaching 130% of AdaptNC’s. As further illustrated in Figures 3 and 4, the absence of replay leads to increased variability in local coverage, which propagates to oscillations in global coverage and necessitates more conservative uncertainty regions. These results highlight the importance of the replay mechanism, which stabilizes coverage under distribution shifts and enables the recovery of tighter, more accurate uncertainty regions.

### 6.2. Social Navigation with Policy Shift

In this case study, we consider a social navigation scenario in which multiple agents move through a shared environment while repeatedly navigating toward randomly assigned

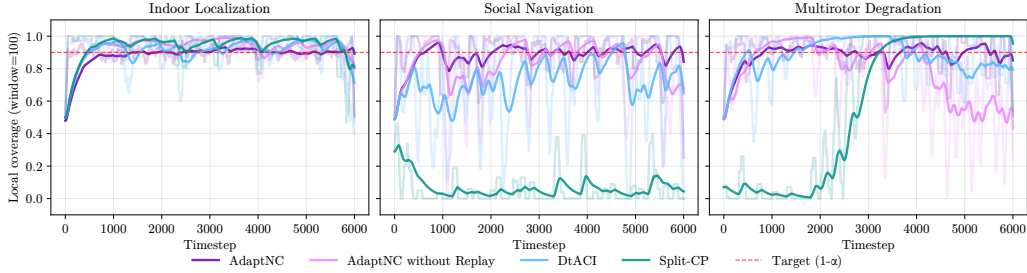


Figure 3. This figure illustrates the **evolution of local coverage over a sliding window of 100 timesteps**. For readability, an exponential moving average is shown, with the raw data in a lighter color. AdaptNC exhibits the lowest variability in local coverage among all methods, indicating stable recovery of tight uncertainty regions under distribution shift. In contrast, AdaptNC without Replay shows substantially higher variability, highlighting the role of the replay mechanism in mitigating coverage shocks induced by distribution shifts.

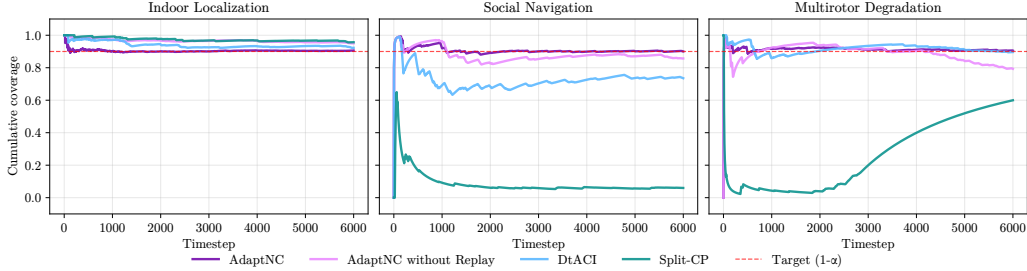


Figure 4. This figure illustrates the **evolution of empirical coverage over the evaluation horizon relative to the target coverage level** (shown in red). The proposed method consistently remains close to the desired coverage across time, whereas baseline methods exhibit pronounced periods of over- or under-coverage and, when recovery occurs, do so only after substantial deviation. This behavior highlights the flexibility of AdaptNC in maintaining calibrated coverage over time by adapting the nonconformity score function, rather than adjusting the threshold alone, enabling tighter uncertainty regions with sustained coverage.

goals. Agent motion follows the social force model of [Helbing & Molnár \(1995\)](#), combining attractive forces toward goals with repulsive interactions from nearby agents and workspace boundaries, where interactions are limited to a finite collaboration radius. In our experiments, eight agents navigate a  $10\text{ m} \times 10\text{ m}$  workspace over 6000 timesteps, receiving new goals upon reaching their current ones. A policy shift is introduced by gradually expanding the collaboration radius from 2 m to 5 m, which alters how agents anticipate and respond to surrounding traffic over time. Trajectory prediction is performed using an LSTM trained under nominal conditions to predict the ego agent’s position five timesteps ahead from the past ten timesteps of observations, including the ego state, ego goal, and relative positions of other agents. At evaluation time, the expanding interaction radius induces a growing mismatch between the predictor’s training distribution and the evolving system behavior, as agents begin to slow down earlier or deviate to avoid more distant neighbors. This unmodeled policy shift gives rise to a distribution shift that degrades the coverage of non-adaptive conformal prediction methods, such as Split CP. Full details of the simulation setup are provided in Appendix D.3.

**Performance Evaluation and Comparative Analysis:** As reported in Table 1, AdaptNC achieves a global coverage of 90.00%, exactly matching the target coverage level of 90%, whereas all baseline methods exhibit undercoverage. Although Split CP produces the smallest uncertainty vol-

ume, it exhibits severe undercoverage, attaining only 5.98% coverage and missing the target level by 84.02%. DtACI also fails to meet the target coverage, missing it by 16.5%, while incurring a significantly larger uncertainty volume than AdaptNC, amounting to 140% of AdaptNC’s volume. This behavior reflects an inherent tradeoff between coverage and volume in DtACI arising from the fixed geometry of its nonconformity score. As shown in Figure 4, baseline methods experience coverage degradation even before the collaboration radius increases at  $t = 2000$ , highlighting the intrinsic difficulty of the multi-agent setting. Local coverage statistics in Figure 3 further reveal intermittent coverage drops for the baselines, whereas AdaptNC maintains coverage consistently close to the target, remaining within one standard deviation of the local coverage target. In contrast, the ablation AdaptNC without Replay exhibits mild undercoverage while producing substantially larger uncertainty regions, corresponding to 160% of AdaptNC’s volume. These results further validate the importance of the replay mechanism for achieving stable, efficient coverage.

### 6.3. Multirotor Tracking under Actuator Degradation

In this case study, we consider a multirotor tracking scenario in which a multirotor platform is tasked with tracking a figure-eight reference trajectory in the  $x$ - $y$  plane at constant altitude. Over the course of operation, the platform experiences stochastic actuator degradation, leading to a gradual loss of control effectiveness. The system is mod-

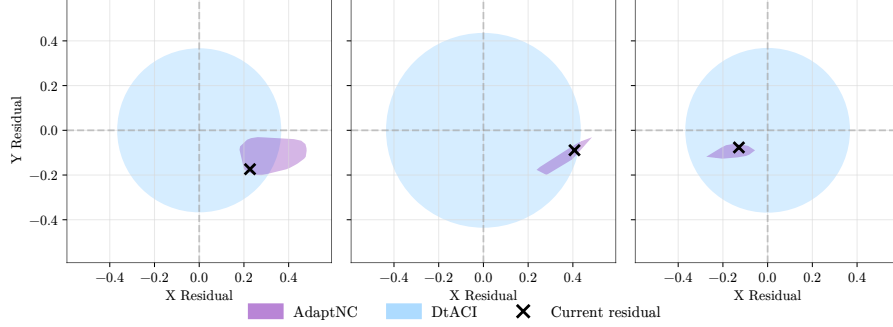


Figure 5. This figure visualizes the uncertainty regions produced by AdaptNC and DtACI at three representative timesteps ( $t \in [720, 1560, 3120]$ ) in the multirotor tracking task, paired with the realized residual at each timestep. The results show that **AdaptNC recovers markedly tighter uncertainty regions** while maintaining coverage. In contrast, DtACI adapts the score threshold, constraining the region geometry and leading to misalignment with the residual distribution in the presence of structural distribution shifts.

Method	Indoor Localization			Social Navigation			Multirotor Navigation		
	Global Cov.	Avg. Volume ↓	Mean Local Cov.	Global Cov.	Avg. Volume ↓	Mean Local Cov.	Global Cov.	Avg. Volume ↓	Mean Local Cov.
AdaptNC (Ours)	<b>90.65%</b>	<b>30.79m<sup>2</sup></b>	<b>90.18% ± 4.10%</b>	<b>90.00%</b>	13.07m <sup>2</sup>	<b>90.18% ± 4.10%</b>	<b>90.17%</b>	<b>0.05m<sup>2</sup></b>	<b>90.22% ± 9.05%</b>
AdaptNC w/o Replay	95.50%	43.09m <sup>2</sup>	94.60% ± 6.61%	85.70%	21.02m <sup>2</sup>	85.34% ± 20.17%	79.58%	0.11m <sup>2</sup>	79.07% ± 24.12%
DtACI	91.97%	43.11m <sup>2</sup>	91.87% ± 10.32%	73.53%	18.22m <sup>2</sup>	73.34% ± 27.31%	89.65%	0.46m <sup>2</sup>	89.25% ± 13.28%
Split CP	95.45%	100.41m <sup>2</sup>	95.28% ± 8.41%	5.98%	<b>0.512m<sup>2</sup></b>	5.92% ± 9.71%	59.97%	0.21m <sup>2</sup>	59.70% ± 45.34%

Table 1. This table contains the proposed evaluation metrics across all methods and case studies. AdaptNC achieves coverage closest to the target level of 90% while maintaining low average uncertainty volumes. In contrast, competing methods exhibit a trade-off between coverage and volume, either attaining coverage targets with high volume, or missing them with small volumes. **AdaptNC achieves the most stable coverage behavior over time**, as evidenced by the lowest standard deviation of local coverage.

eled using linearized 12-dimensional multirotor dynamics following Dixit et al. (2023), where actuator degradation is captured through a multiplicative health matrix acting on the commanded control inputs. Each actuator’s effectiveness evolves stochastically, reflecting cumulative fault propagation commonly considered in predictive maintenance models (Shen et al., 2024). Trajectory prediction is performed using an LSTM trained under nominal conditions to predict future planar motion from a fixed window of past states. At test time, the growing mismatch between commanded and effective inputs induces a progressive shift in the system behavior, thereby violating the predictor’s implicit assumption of full actuation. Evaluation is conducted over a single continuous rollout of 6000 time steps under degradation, allowing the resulting prediction bias and policy shift to accumulate and providing a challenging benchmark for evaluating adaptive uncertainty quantification. Additional experimental details are provided in Appendix D.2.

**Performance Evaluation and Comparative Analysis:** As shown in Table 1, both AdaptNC (90.17%) and DtACI (89.65%) achieve coverage close to the 90% target, however DtACI requires a region volume 920% greater than that of AdaptNC. We see in Figure 5 that shape adaptation enables significantly tighter conformal prediction regions while maintaining coverage. In contrast, Split CP exhibits pronounced undercoverage due to its non-adaptive calibration under distribution shift. The importance of replay is further illustrated by AdaptNC without replay, which shows systematic undercoverage and increased temporal variability in local and global coverage (Figures 3 and 4). These results

continue to highlight the importance of replay in stabilizing coverage under strong distribution shifts.

**Results Summary:** Across all three case studies, AdaptNC maintains coverage close to the target level under structural distribution shifts while recovering significantly tighter uncertainty regions than competing methods. By jointly adapting the nonconformity score and threshold, AdaptNC avoids the conservatism of threshold-only adaptation and the undercoverage of non-adaptive baselines, with the replay mechanism mitigating coverage shocks and stabilizing local coverage. This behavior is also evident in the expert weight dynamics highlighted in Figures 10, 11, and 12, with AdaptNC exhibiting faster reweighting than DtACI and AdaptNC without Replay. Further details on this analysis could be found in Appendices D.2, D.3, and, D.4.

## 7. Conclusion

We present AdaptNC, an online conformal prediction method that adapts nonconformity scores under distribution shift. AdaptNC leverages a reweighted data distribution to balance reliance on past data and introduces a replay mechanism to stabilize adaptation and maintain coverage as scores evolve. We establish theoretical regret and long-term coverage guarantees and validate the approach on three robotics case studies involving **environmental change, multi-agent interaction, and system degradation**. Across all settings, AdaptNC achieves coverage closer to the target level with lower uncertainty volume than competing methods, demonstrating its efficacy under distribution shift. Future work will address the limitations discussed in Appendix A.

## Impact Statement

This paper presents a method for uncertainty quantification in autonomous systems operating under distribution shift. Our work is primarily methodological, focused on improving conformal prediction techniques, we recognize several potential societal implications. First, our method can improve the safety of the general public through enabling safer autonomy. The use of optimized non-conformity scores can help ensure that robots of the future offer high-performance through decreased conservatism while maintaining coverage.

## References

Barber, C. B., Dobkin, D. P., and Huhdanpaa, H. The quickhull algorithm for convex hulls. *ACM Transactions on Mathematical Software*, 22(4):469–483, December 1996. ISSN 0098-3500. doi: 10.1145/235815.235821. URL <https://dl.acm.org/doi/10.1145/235815.235821>.

Barber, R. F., Candès, E. J., Ramdas, A., and Tibshirani, R. J. Predictive inference with the jackknife+, May 2020. URL <http://arxiv.org/abs/1905.02928>. arXiv:1905.02928 [stat].

Barber, R. F., Candès, E. J., Ramdas, A., and Tibshirani, R. J. Conformal prediction beyond exchangeability. *The Annals of Statistics*, 51(2):816–845, April 2023. ISSN 0090-5364, 2168-8966. doi: 10.1214/23-AOS2276. URL <https://doi.org/10.1214/23-AOS2276>.

Bastani, O., Gupta, V., Jung, C., Noarov, G., Ramalingam, R., and Roth, A. Practical Adversarial Multivalid Conformal Prediction. October 2022. URL <https://openreview.net/forum?id=QNjyrDBx6tz>.

Binny, A. E. and Dixit, A. Who Moved My Distribution? Conformal Prediction for Interactive Multi-Agent Systems, November 2025. URL <http://arxiv.org/abs/2511.11567>. arXiv:2511.11567 [eess].

Braun, S., Aolaritei, L., Jordan, M. I., and Bach, F. Minimum Volume Conformal Sets for Multivariate Regression, March 2025. URL <http://arxiv.org/abs/2503.19068>. arXiv:2503.19068 [stat].

Cadre, B. Kernel estimation of density level sets. *Journal of Multivariate Analysis*, 97(4):999–1023, April 2006. ISSN 0047259X. doi: 10.1016/j.jmva.2005.05.004. URL <https://linkinghub.elsevier.com/retrieve/pii/S0047259X05000825>.

Clarke, R. H. A statistical theory of mobile-radio reception. *Bell system technical journal*, 47(6):957–1000, 1968.

Cleaveland, M., Lee, I., Pappas, G. J., and Lindemann, L. Conformal Prediction Regions for Time Series Using Linear Complementarity Programming. *Proceedings of the AAAI Conference on Artificial Intelligence*, 38(19):20984–20992, March 2024. ISSN 2374-3468. doi: 10.1609/aaai.v38i19.30089. URL <https://ojs.aaai.org/index.php/AAAI/article/view/30089>.

Dixit, A., Lindemann, L., Wei, S. X., Cleaveland, M., Pappas, G. J., and Burdick, J. W. Adaptive Conformal Prediction for Motion Planning among Dynamic Agents. In *Proceedings of The 5th Annual Learning for Dynamics and Control Conference*, pp. 300–314. PMLR, June 2023. URL <https://proceedings.mlr.press/v211/dixit23a.html>.

Gao, C., Shan, L., Srinivas, V., and Vijayaraghavan, A. Volume Optimality in Conformal Prediction with Structured Prediction Sets. June 2025. URL <https://openreview.net/forum?id=oNDhnGrD51&noteId=7kR09SC5BY>.

Gibbs, I. and Candès, E. Adaptive Conformal Inference Under Distribution Shift. In *Advances in Neural Information Processing Systems*, volume 34, pp. 1660–1672. Curran Associates, Inc., 2021. URL <https://proceedings.neurips.cc/paper/2021/hash/0d441de75945e5acbc865406fc9a2559-Abstract.html>.

Gibbs, I. and Candès, E. J. Conformal Inference for Online Prediction with Arbitrary Distribution Shifts. *Journal of Machine Learning Research*, 25(162):1–36, 2024. ISSN 1533-7928. URL <http://jmlr.org/papers/v25/22-1218.html>.

Gudmundson, M. Correlation model for shadow fading in mobile radio systems. *Electronics letters*, 27(23):2145–2146, 1991.

Helbing, D. and Molnár, P. Social force model for pedestrian dynamics. *Physical Review E*, 51(5):4282–4286, May 1995. doi: 10.1103/PhysRevE.51.4282. URL <https://link.aps.org/doi/10.1103/PhysRevE.51.4282>.

Jakes, W. C. and Cox, D. C. *Microwave mobile communications*. Wiley-IEEE press, 1994.

Kiyani, S., Pappas, G., and Hassani, H. Length Optimization in Conformal Prediction. *Advances in Neural Information Processing Systems*, 37:99519–99563, December 2024. doi: 10.52202/079017-3158. URL <https://doi.org/10.52202/079017-3158>.

Kuipers, T., Tumu, R., Yang, S., Kazemi, M., Mangharam, R., and Paoletti, N. Conformal Off-Policy Prediction for Multi-Agent Systems. In *2024 IEEE 63rd Conference on Decision and Control (CDC)*, pp. 1067–1074, December 2024. doi: 10.1109/CDC56724.2024.10886791. URL <https://ieeexplore.ieee.org/document/10886791>. ISSN: 2576-2370.

Lei, J., G’Sell, M., Rinaldo, A., Tibshirani, R. J., and Wasserman, L. Distribution-Free Predictive Inference for Regression. *Journal of the American Statistical Association*, 113(523):1094–1111, July 2018. ISSN 0162-1459. doi: 10.1080/01621459.2017.1307116. URL <https://doi.org/10.1080/01621459.2017.1307116>. eprint: <https://doi.org/10.1080/01621459.2017.1307116>.

Lindemann, L., Cleaveland, M., Shim, G., and Pappas, G. J. Safe Planning in Dynamic Environments Using Conformal Prediction. *IEEE Robotics and Automation Letters*, 8(8):5116–5123, August 2023. ISSN 2377-3766. doi: 10.1109/LRA.2023.3292071. URL <https://ieeexplore.ieee.org/abstract/document/10172259>.

Lindemann, L., Zhao, Y., Yu, X., Pappas, G. J., and Deshmukh, J. V. Formal verification and control with conformal prediction: Practical safety guarantees for autonomous systems. *IEEE Control Systems*, 45(6):72–122, 2025. doi: 10.1109/MCS.2025.3611545.

Lindqvist, B., Mansouri, S. S., Agha-mohammadi, A.-a., and Nikolakopoulos, G. Nonlinear MPC for Collision Avoidance and Control of UAVs With Dynamic Obstacles. *IEEE Robotics and Automation Letters*, 5(4):6001–6008, October 2020. ISSN 2377-3766. doi: 10.1109/LRA.2020.3010730. URL <https://ieeexplore.ieee.org/abstract/document/9145644>.

Parzen, E. On Estimation of a Probability Density Function and Mode. *The Annals of Mathematical Statistics*, 33(3):1065–1076, 1962. ISSN 0003-4851. URL <https://www.jstor.org/stable/2237880>.

Polyanskiy, Y. and Wu, Y. *Information theory: from coding to learning*. Cambridge University Press, Cambridge, United Kingdom ; New York, NY, 2025. ISBN 978-1-108-83290-8 978-1-108-96635-1. doi: 10.1017/9781108966351.

Rappaport, T. S. *Wireless communications: Principles and practice*, 2/E. Pearson Education India, 2010.

Scott, D. W. On optimal and data-based histograms. *Biometrika*, 66(3):605–610, 1979. ISSN 0006-3444, 1464-3510. doi: 10.1093/biomet/66.3.605. URL <https://academic.oup.com/biomet/article-lookup/doi/10.1093/biomet/66.3.605>.

Shen, F.-y., Li, W., Jiang, D.-n., and Mao, H.-j. Autonomous predictive maintenance of quadrotor uav with multi-actuator degradation. *The Aeronautical Journal*, 128(1326):1789–1813, 2024.

Silverman, B. W. Weak and Strong Uniform Consistency of the Kernel Estimate of a Density and its Derivatives. *The Annals of Statistics*, 6(1):177–184, 1978. ISSN 0090-5364. URL <https://www.jstor.org/stable/2958700>.

Silverman, B. W. *Density Estimation for Statistics and Data Analysis*. CRC Press, April 1986. ISBN 978-0-412-24620-3.

Tayal, M., Singh, A., Kolathaya, S., and Bansal, S. A physics-informed machine learning framework for safe and optimal control of autonomous systems. In *Forty-second International Conference on Machine Learning*, 2025. URL <https://openreview.net/forum?id=SrfwiloGQF>.

Tibshirani, R. J., Foygel Barber, R., Candes, E., and Ramdas, A. Conformal Prediction Under Covariate Shift. In *Advances in Neural Information Processing Systems*, volume 32. Curran Associates, Inc., 2019. URL <https://papers.nips.cc/paper/2019/hash/8fb21ee7a2207526da55a679f0332de2-Abstract.html>.

Tumu, R., Lindemann, L., Nghiem, T., and Mangharam, R. Physics Constrained Motion Prediction with Uncertainty Quantification. In *2023 IEEE Intelligent Vehicles Symposium (IV)*, pp. 1–8, Anchorage, AK, USA, June 2023. IEEE. ISBN 979-8-3503-4691-6. doi: 10.1109/IV55152.2023.10186812. URL <https://ieeexplore.ieee.org/document/10186812/>.

Tumu, R., Cleaveland, M., Mangharam, R., Pappas, G., and Lindemann, L. Multi-modal conformal prediction regions by optimizing convex shape templates. In *Proceedings of the 6th Annual Learning for Dynamics & Control Conference*, pp. 1343–1356. PMLR, June 2024. URL <https://proceedings.mlr.press/v242/tumu24a.html>.

Vaart, A. W. V. D. *Asymptotic Statistics*. Cambridge University Press, 1 edition, October 1998. ISBN 978-0-511-80225-6 978-0-521-49603-2 978-0-521-78450-4. doi: 10.1017/CBO9780511802256. URL <https://www.cambridge.org/core/product/identifier/9780511802256/type/book>.

Vovk, V., Gammerman, A., and Shafer, G. *Algorithmic Learning in a Random World*. Springer International Publishing, Cham, 2022. ISBN 978-3-031-06649-1 978-3-031-06649-8. doi: 10.1007/978-3-031-06649-8.

URL <https://link.springer.com/10.1007/978-3-031-06649-8>.

Yang, S., Pappas, G. J., Mangharam, R., and Lindemann, L. Safe Perception-Based Control Under Stochastic Sensor Uncertainty Using Conformal Prediction. In *2023 62nd IEEE Conference on Decision and Control (CDC)*, pp. 6072–6078, December 2023. doi: 10.1109/CDC49753. 2023.10384075. URL <https://ieeexplore.ieee.org/abstract/document/10384075>.

Zaffran, M., Feron, O., Goude, Y., Josse, J., and Dieuleveut, A. Adaptive Conformal Predictions for Time Series. In *Proceedings of the 39th International Conference on Machine Learning*, pp. 25834–25866. PMLR, June 2022. URL <https://proceedings.mlr.press/v162/zaffran22a.html>.

## Appendix Contents

<b>A</b>	<b>Limitations</b>	<b>13</b>
<b>B</b>	<b>Method</b>	<b>14</b>
B.1	Score Optimization Algorithm	14
B.2	AdaptNC Algorithm	14
B.3	Dynamically Tuned Adaptive Conformal Inference (DtACI)	14
B.4	High Density Region Identification	14
<b>C</b>	<b>Theoretical Guarantees</b>	<b>18</b>
C.1	Regret Guarantee	18
C.2	Long Term Coverage	18
C.3	Score Function Stability	18
<b>D</b>	<b>Experiments</b>	<b>20</b>
D.1	Gaussian Mixture Model	20
D.2	Indoor Localization	22
D.3	Social Navigation	26
D.4	Multirotor Tracking	30

## A. Limitations

While AdaptNC demonstrates the ability to recover tight, valid uncertainty regions under distribution shift, it remains, as with other adaptive conformal prediction methods, susceptible to producing trivial uncertainty sets. Although such sets are not entirely uninformative, as they indicate that future observations are likely to fall outside the previously observed support and that the system may be undergoing a regime change, they nonetheless represent a limitation. To further examine this behavior, we report the **percentage of vacuous coverage timesteps** for each method in Table 2, defined as  $\frac{1}{T} \sum_{t=0}^T \mathbb{1}\{\hat{q}_{t,1-\alpha} = \infty\}$ , which quantifies the frequency with which a method yields uninformative, unbounded uncertainty regions.

Method	Indoor Localization	Social Navigation	Multirotor Navigation
AdaptNC	11.51%	40.42%	33.65%
AdaptNC w/o Replay	11.93%	24.52%	22.82%
DtACI	15.67%	21.17%	28.77%
Split CP	0.00%	0.00%	0.00%

Table 2. This table lists the **percentage of timesteps exhibiting vacuous coverage** for each method across all case studies. **Methods incorporating temporal adaptation exhibit a nonzero frequency of vacuous coverage.**

Table 2 shows that Split CP does not exhibit vacuous coverage at any time step, as it lacks the ability to adapt over time. In contrast, all methods incorporating temporal adaptation, including DtACI, exhibit a nonzero fraction of timesteps in which trivial uncertainty sets are recovered. Although AdaptNC achieves the lowest proportion of vacuous coverage timesteps for the Indoor Localization and Social Navigation tasks, the differences among the three adaptive methods are relatively modest. For the Multirotor Navigation task, AdaptNC attains the highest fraction of vacuous coverage timesteps; however, the remaining adaptive methods also display comparably high proportions. These results indicate that vacuous coverage is a shared limitation across all adaptive conformal prediction methods considered in this study.

## B. Method

### B.1. Score Optimization Algorithm

---

**Algorithm 1** OptimizeScore: Score Parameter Optimization

**Require:** History buffer  $\mathcal{H}_t^\omega$ , current parameters  $\theta$ , target miscoverage rate  $\alpha$ 

- 1: Generate high-density points  $\hat{R}_t$  covering proportion  $1 - \alpha$  of density mass through Algorithm 4
- 2: Fit shape template  $\mathcal{S}$  using QuickHull algorithm on  $\hat{R}_t$
- 3:  $\theta_{t+1} \leftarrow$  parameters encoding shape templates  $\{\mathcal{S}\}$
- 4: **Return:** Updated parameters  $\theta_{t+1}$

---

### B.2. AdaptNC Algorithm

---

**Algorithm 2** AdaptNC Algorithm

**Require:** Target miscoverage rate  $\alpha$ , adaptation interval  $t_s$ , initial parameters  $\theta_0$ , DtACI expert gammas  $\Gamma = [\gamma_1, \dots, \gamma_k]$ , window size  $W$ , learning rate  $\eta$ , calibration data  $\mathcal{D}_{cal}$ 

 Initialize history buffer  $\mathcal{H} \leftarrow \emptyset$ 

 Fit initial conformal region with  $\theta_0$  on  $\mathcal{D}_{cal}$ 

 Initialize DtACI with  $s(\cdot; \theta_0)$ ,  $\alpha$ ,  $\Gamma$ ,  $W$ ,  $\eta$ ,  $\mathcal{D}_{cal}$ 
**for**  $t = 1, 2, \dots, T$  **do**

 Observe  $X_t$ , produce prediction  $\hat{Y}_t$ , observe  $Y_t$ 

 Compute score  $s_t = s(X_t, Y_t; \theta_t)$ 

 Append  $(X_t, Y_t, s_t)$  to  $\mathcal{H}$ 

 Update DtACI with  $(X_t, Y_t)$  to obtain  $\bar{\alpha}_t$ 

 Obtain new threshold:  $q_{1-\alpha_t, \mathcal{D}}$ 

 Output prediction region  $\hat{C}_t(X_t; \theta_t, q_{1-\alpha_t, \mathcal{D}})$ 
**if**  $t \bmod t_s = 0$  **then**

 Compute distribution  $\mathcal{H}_t^\omega$  using Equation (4)

 $\theta_{t+1} \leftarrow \text{OPTIMIZESCORE}(\mathcal{H}_t^\omega, \theta_t, \alpha)$ 

 Re-initialize DtACI with score function  $s(\cdot; \theta_{t+1})$ 
**for** each  $(X_i, Y_i) \in [t - w + 1, t]$  **do**

 Update experts and expert weights with  $(X_i, Y_i)$ 
**end for**
**end if**
**end for**

### B.3. Dynamically Tuned Adaptive Conformal Inference (DtACI)

See Algorithm 3.

### B.4. High Density Region Identification

We analyze the convergence properties of the MCKDE method. Let the true underlying density function be denoted as  $f$  on  $\mathbb{R}^d$ . For a specified miscoverage rate  $\alpha \in (0, 1)$ , the true High-Density Region (HDR) is defined as the level set  $R_b = \{z \in \mathbb{R}^d : f(z) \geq b\}$ . We aim to show that the estimated region  $\hat{R}_{N,M}$  converges to the true region  $R_\alpha$  as both the number of samples  $N$  used to construct the KDE and the number of Monte Carlo samples  $M$  increase.

The procedure described in Algorithm 4 aims to estimate this region using a Kernel Density Estimator (KDE)  $\hat{f}_N$  constructed from  $N$  reweighted samples drawn from the true distribution. This reweighted empirical distribution is considered to be the "true" distribution for the purpose of the monte-carlo sampling.

From this distribution, we draw  $M$  Monte Carlo samples  $\{z_1, \dots, z_M\}$ . These are then scored using the KDE to obtain density estimates  $\xi_i = \hat{f}_N(z_i)$ . The threshold  $\hat{\tau}$  is determined as the  $\alpha$ -quantile of these scores,  $\hat{\tau} = \text{Quantile}(\{\xi_i\}_{1 \leq i \leq M}, \alpha)$ , and the estimated HDR is defined as  $\hat{R}_{N,M} = \{z_i : \xi_i \geq \hat{\tau}\}$ .

---

**Algorithm 3** Dynamically tuned Adaptive Conformal Inference (DtACI) (Gibbs & Candès, 2024, Algorithm 2)

---

**Require:** Observed values  $\{\beta_t\}_{1 \leq t \leq T}$ , set of candidate  $\gamma$  values  $\{\gamma_i\}_{1 \leq i \leq k}$ , starting points  $\{\alpha_1^i\}_{1 \leq i \leq k}$ , and parameters  $\sigma$  and  $\eta$ .

- 1:  $w_1^i \leftarrow 1, 1 \leq i \leq k;$
- 2: **for**  $t = 1, 2, \dots, T$  **do**
- 3:   Define the probabilities  $p_t^i := w_t^i / \sum_{1 \leq j \leq k} w_t^j, \forall 1 \leq i \leq k;$
- 4:   Output  $\bar{\alpha}_t = \sum_{1 \leq i \leq k} p_t^i \alpha_t^i;$
- 5:    $\bar{w}_t^i \leftarrow w_t^i \exp(-\eta \ell(\beta_t, \alpha_t^i)), \forall 1 \leq i \leq k;$
- 6:    $\bar{W}_t \leftarrow \sum_{1 \leq i \leq k} \bar{w}_t^i;$
- 7:    $w_{t+1}^i \leftarrow (1 - \sigma) \bar{w}_t^i + \bar{W}_t \sigma / k;$
- 8:    $\mathbf{err}_t^i := \mathbf{1}\{Y_t \notin \hat{C}_t(\alpha_t^i; \theta_t, \mathcal{D}_t)\}, \forall 1 \leq i \leq k;$
- 9:    $\mathbf{err}_t := \mathbf{1}\{Y_t \notin \hat{C}_t(\bar{\alpha}_t; \theta_t, \mathcal{D}_t)\};$
- 10:    $\alpha_{t+1}^i = \alpha_t^i + \gamma_i(\alpha - \mathbf{err}_t^i), \forall 1 \leq i \leq k;$
- 11: **end for**

---

**Theorem B.1** (Consistency of MCKDE). *Given the following conditions:*

1. *The density  $f$  is bounded and twice continuously differentiable.*
2. *The gradient of the density has strictly positive magnitude,  $\inf_{f^{-1}(\{t\})} \|\nabla f\| > 0$  for almost every  $t \geq 0$ .*
3. *The measure  $\lambda(f^{-1}([t_\alpha - \epsilon, t_\alpha + \epsilon])) \rightarrow 0$  as  $\epsilon \rightarrow 0$ , and  $\lambda(f^{-1}(0, \epsilon]) \rightarrow 0$  as  $\epsilon \rightarrow 0$ .*
4. *The kernel function  $K$  is the gaussian kernel.*
5. *The bandwidth of the KDE is selected according to the rules of Scott (1979) or Silverman (1986).*

Then, as  $N \rightarrow \infty$  and  $M \rightarrow \infty$ , the estimated region  $\hat{R}_{N,M}$  converges to the true region  $R_\alpha$  in probability:

$$\lambda(\hat{R}_{N,M} \Delta R_\alpha) \xrightarrow{P} 0 \quad (9)$$

*Proof.* We note that the procedure described in Algorithm 4 can be viewed as a two-step estimation process. First, we estimate the density function  $f$  using a Kernel Density Estimator (KDE)  $\hat{f}_N$  based on  $N$  reweighted samples. Second, we use Monte Carlo sampling to estimate the level set of the KDE,  $\hat{R}_{N,M}$ . This two-step process allows us to analyze the convergence properties of each step separately.

**Step 1: Convergence of the KDE** Under the assumptions stated in Theorem B.1, particularly the smoothness of  $f$  and the choice of bandwidth, Theorem B.3 shows that the KDE  $\hat{f}_N$  converges to the true density  $f$  almost surely as  $N \rightarrow \infty$ . This implies the following:

$$\lim_{N \rightarrow \infty} \|\hat{f}_N - f\| = 0 \quad (10)$$

Therefore, as  $N$  goes to  $\infty$ , the estimated density  $\hat{f}_N$  is the same as the true density  $f$ .

We must also show that the level sets of  $\hat{f}_N$  converge to those of  $f$ . Let  $R_\alpha = \{x : f(x) \geq t_\alpha\}$  be the true high-density region, where  $t_\alpha$  is the unique threshold such that  $\mathbb{P}_{Z \sim f}(Z \in R_\alpha) = 1 - \alpha$ . Let  $R_N = \{x \in \mathbb{R}^d : \hat{f}_N(x) \geq t_N\}$  denote the level set estimate, where  $t_N$  is the unique threshold such that the region contains exactly  $1 - \alpha$  of the probability mass defined by  $\hat{f}_N$ :

$$\mathbb{P}_{Z \sim \hat{f}_N}(Z \in R_N) = \int_{\{z : \hat{f}_N(z) \geq t_N\}} \hat{f}_N(z) dz = 1 - \alpha \quad (11)$$

By Corollary B.5, we have that the measure of the symmetric difference between the level sets converges in probability:

$$\lambda(R_N \Delta R_\alpha) \xrightarrow{P} 0 \text{ as } N \rightarrow \infty \quad (12)$$

**Algorithm 4** Monte Carlo Kernel Density Estimation (MCKDE)

---

```

1: Input: Dataset  $X \in \mathbb{R}^{N \times d}$ , sample weights  $w \in \mathbb{R}^N$ , Monte Carlo samples  $M$ , miscoverage rate  $\alpha$ , bandwidth factor  $\beta$ .
2: Output: Set of high-density samples  $\hat{R}_{N,M}$ .
3: // 1. Bandwidth Selection
4: if bandwidth method is “Scott” then
5:    $h \leftarrow N^{\frac{-1}{d+4}}$ 
6: else if bandwidth method is “Silverman” then
7:    $h \leftarrow \left( \frac{N(d+2)}{4} \right)^{\frac{-1}{d+4}}$ 
8: end if
9:  $h \leftarrow h \times \beta$ 
10: // 2. Fit Kernel Density Estimator
11: Fit weighted Gaussian KDE  $\hat{f}_N$  using  $(X, w)$ 
12: // 3. Monte Carlo Sampling & Scoring
13: Draw  $M$  samples  $\mathcal{Z} = \{z_1, \dots, z_M\}$  where  $z_i \sim \hat{f}_N$ 
14: Calculate density scores  $\xi_i \leftarrow \hat{f}_N(z_i)$  for  $i = 1, \dots, M$ 
15: // 4. Thresholding
16: Let  $\tau$  be the  $\alpha$ -quantile of the set  $\{\xi_1, \dots, \xi_M\}$ 
17:  $\hat{R}_{N,M} \leftarrow \{z_i \in \mathcal{Z} \mid \xi_i \geq \tau\}$ 
18: return  $\hat{R}_{N,M}$ 

```

---

**Step 2: Convergence of the Level Set Estimation**

We now analyze the error introduced by the Monte Carlo approximation. The high density region is the minimum set of points where the sum of the scores equals  $1 - \alpha$ . In order to assemble the volume minimizing set, we would clearly select the points with the highest scores, leading to the thresholding condition above. Let  $\xi = \hat{f}_N(Z)$  be the random variable representing the density score of a sample drawn from  $\hat{f}_N$ . The cumulative distribution function (CDF) of the scores is given by  $G_N(t) = \mathbb{P}(\xi \leq t)$ . We can express the thresholding condition in terms of the CDF:

$$G_N(t_N) = \mathbb{P}(\xi \leq t_N) = \alpha \quad (13)$$

Thus, the theoretical threshold  $t_N$  is exactly the  $\alpha$ -quantile of the distribution of density scores.

The algorithm approximates the score CDF by drawing  $M$  i.i.d. samples  $z_1, \dots, z_M \sim \hat{f}_N$  and computing their scores  $\xi_i = \hat{f}_N(z_i)$ . Let  $\hat{G}_M(t) = \frac{1}{M} \sum_{i=1}^M \mathbb{I}(\xi_i \leq t)$  be the empirical cumulative distribution function of the scores. The algorithm selects  $\hat{\tau}_M$  as the empirical  $\alpha$ -quantile:  $\hat{\tau}_M = \hat{G}_M^{-1}(\alpha)$ , defining the estimated region  $\hat{R}_{N,M} = \{x : \hat{f}_N(x) \geq \hat{\tau}_M\}$ .

By the Glivenko-Cantelli theorem (Theorem B.4), the empirical CDF converges uniformly to the true CDF  $G_N$  almost surely as  $M \rightarrow \infty$ . Therefore, the empirical quantile converges to the true quantile:

$$|\hat{\tau}_M - t_N| \xrightarrow{a.s.} 0 \quad (14)$$

Since we utilize a Gaussian kernel, the estimated density  $\hat{f}_N$  is continuous and has no flat regions. Therefore, the measure of the symmetric difference between the level sets is continuous with respect to the threshold. The convergence of the threshold implies the convergence of the regions:

$$\lambda(\hat{R}_{N,M} \Delta R_N) \leq \lambda(\{x : |\hat{f}_N(x) - t_N| \leq |\hat{\tau}_M - t_N|\}) \xrightarrow{a.s.} 0 \quad (15)$$

**Conclusion** Combining the results, we have that as  $N \rightarrow \infty$ :  $\hat{f}_N \rightarrow f$  (almost surely), and that as  $M \rightarrow \infty$ :  $\hat{R}_{N,M} \rightarrow R_N$ , where the set  $R_N$  is defined by the KDE  $\hat{f}_N$ . Since  $\hat{f}_N$  converges to  $f$ , the set  $R_N$  converges to the true set  $R_\alpha$ . Therefore, we conclude that:

$$\lambda(\hat{R}_{N,M} \Delta R_\alpha) \xrightarrow{P} 0 \quad (16)$$

□

*Remark B.2.* The above proof shows that under the same conditions as Theorem B.1, the MCKDE procedure is asymptotically correct, in that it will approach the true level set as the number of samples goes to infinity.

**Theorem B.3** (KDE Convergence, Theorem A, [Silverman \(1978\)](#)). *Assuming that the conditions in Theorem B.1 hold, the Kernel Density Estimator  $\hat{f}_N$  converges uniformly to the true density  $f$  almost surely as  $N \rightarrow \infty$ :*

$$\limsup_{N \rightarrow \infty} |\hat{f}_N(x) - f(x)| = 0 \quad (17)$$

**Theorem B.4** (Glivenko-Cantelli Theorem as written in [Vaart \(1998\)](#)). *If  $X_1, X_2, \dots, X_n$  are independent and identically distributed random variables with cumulative distribution function  $f$ , and empirical distribution function  $f_n$ , then:*

$$\|f_n - f\|_\infty \xrightarrow{as} 0 \quad (18)$$

**Corollary B.5** (Corollary 2.1 from [Cadre \(2006\)](#)). *This corollary is a consequence of Cadre (2006, Theorem 2.1) Let  $d \geq 2$  be the dimension of the data, and  $(a_N)_N$  be a sequence of positive real numbers such that  $a_N \rightarrow 0$ . Let  $t^{(p)}$  be the unique real number such that  $\lambda_f(L(f, t^{(p)})) = p$ , and  $t_N^{(p)}$  be the unique real number such that  $\lambda_{\hat{f}_N}(L(\hat{f}_N, t_N^{(p)})) = p$ . If the assumptions of Theorem B.1 hold, then for almost every  $t \geq 0$  we have that:*

$$\lambda(\hat{R}_{M,N,p} \Delta R_p) \xrightarrow{P} \frac{\sqrt{t_N^{(p)}}}{\sqrt{Nh^d} \varphi_N} \sqrt{\frac{2t}{\pi} \int K^2 d\lambda} \quad (19)$$

Where  $\varphi_N = a_N / \lambda(\hat{R}_{M,N,p} - \hat{R}_{M,N,p+a_N})$

Note that in this corollary, the square root of the kernel term is a constant that depends on the choice of kernel, and the term  $\sqrt{Nh^d}$  grows to infinity as  $N$  increases, ensuring that the estimation error decreases with larger sample sizes. The term  $t_N^{(p)}$  represents the density threshold corresponding to the level set, which is bounded for a well-defined density function. Thus, the corollary indicates that the estimation error diminishes as the sample size increases. The asymptotic behaviour described in Corollary B.5 is that

$$\lambda(\hat{R}_{M,N,p} \Delta R_p) \xrightarrow{P} O\left(1/\sqrt{Nh^d}\right) \quad (20)$$

## C. Theoretical Guarantees

### C.1. Regret Guarantee

We present the theorem that yields Remark 5.2

**Theorem C.1** (Theorem 4, (Gibbs & Candès, 2024)). *Let  $\gamma_{\max} := \max_{1 \leq i \leq k} \gamma_t$  and assume that  $\gamma_1 < \gamma_2 < \dots < \gamma_k$  where  $\gamma_{i+1}/\gamma_i \leq 2$  for all  $1 < i \leq k$ , and that  $\ell(\beta_t, \theta) := \alpha(\beta_t - \theta) - \min\{0, \beta_t - \theta\}$ . Then, for any window  $W = [r, s] \in [T]$  and any sequence  $\alpha_r^*, \dots, \alpha_s^* \in [0, 1]$ ,*

$$\begin{aligned} \frac{1}{|W|} \sum_{t=r}^s \ell((\beta_t, \bar{\alpha}_t)) - \frac{1}{|W|} \sum_{t=r}^s \ell((\beta_t, \alpha_t^*)) &\leq \\ \frac{\log(k/\sigma) + 2\sigma|W|}{\eta|W|} + \frac{\eta}{|W|} \sum_{t=r}^s \mathbb{E}[\ell(\beta_t, \alpha_t)^2] + \\ 4(1 + \gamma_{\max})^2 \max \left\{ \sqrt{\frac{\sum_{t=r+1}^s |\alpha_t^* - \alpha_{t-1}^*| + 1}{|W|}}, \gamma_1 \right\}. \end{aligned} \quad (21)$$

The bound of the error presented here can be written in simpler form for specific choices of  $\sigma$  and  $\eta$ . Specifically,  $\eta = \sqrt{\frac{\log(2k|W|) + 1}{\sum_{t=r}^s \mathbb{E}[\ell(\beta_t, \alpha_t)^2]}}$  and  $\sigma = 1/(2|W|)$

$$\frac{1}{|W|} \sum_{t=r}^s \ell((\beta_t, \bar{\alpha}_t)) - \frac{1}{|W|} \sum_{t=r}^s \ell((\beta_t, \alpha_t^*)) \leq O\left(\frac{\log(|W|)}{|W|}\right) + O\left(\sqrt{\frac{\sum_{t=r+1}^s |\alpha_t^* - \alpha_{t-1}^*| + 1}{|W|}}, \gamma_1\right). \quad (22)$$

This derivation is due to [Gibbs & Candès \(2024\)](#)

### C.2. Long Term Coverage

**Theorem C.2** (Theorem 6, (Gibbs & Candès, 2024)). *Consider a modified version of Algorithm 3 in which on iteration  $t$  the parameters  $\eta$  and  $\sigma$  are replaced by values  $\eta_t$  and  $\sigma_t$ . Let  $\gamma_{\min} := \min_i \gamma_i$ ,  $\gamma_{\max} := \max_i \gamma_i$ , and that  $\lim_{t \rightarrow \infty} \eta_t = \lim_{t \rightarrow \infty} \sigma_t = 0$ . Then,*

$$\lim_{T \rightarrow \infty} \frac{1}{T} \sum_{t=1}^T \text{err}_t \xrightarrow{a.s.} \alpha$$

where the expectation is over the randomness in the randomized variant of DtACI and the data  $\beta_1, \dots, \beta_T$  can be viewed as fixed.

### C.3. Score Function Stability

**Theorem 5.3** (Score Function Stability). *Consider the same modified version of Algorithm 3 as in Theorem C.2. Let  $\lim_{t \rightarrow \infty} \eta_t = \sigma_t = 0$ , and the number of data samples and Monte Carlo samples in Algorithm 4  $N, M \rightarrow \infty$ . Then the non-conformity score functions will stabilize:  $s(\cdot; \theta_t) = s(\cdot; \theta_{t+1})$  as  $t \rightarrow \infty$ .*

*Proof.* The procedure described in Algorithm 1 creates a non-conformity score through a three step procedure: (1) Reweighting, (2) High-Density Region Identification, and (3) Convex Hull creation.

The reweighting procedure uses the expert weights  $\gamma_i$  and the weights  $w_t^i$  to create an exponentially weighted distribution  $\mathcal{H}_t^w$ . While we ordinarily have no guarantees on the evolution of these weights, under the assumption that  $\eta_t, \sigma_t \rightarrow 0$ , the updates in the DtACI algorithm yield identical weights across timesteps  $w_{t+1}^i = w_t^i$ . Thus, the reweighted distributions  $\mathcal{H}_t^w$  and  $\mathcal{H}_{t+1}^w$  will be the same as  $t \rightarrow \infty$ .

For each distribution  $\mathcal{H}_t^w$ , the High-Density Region identification procedure uses a kernel density estimator to estimate the density, and then identifies the High-Density Region  $\hat{R}_t$  that contains  $1 - \alpha$  mass of the estimated density. By Theorem B.1, the High-Density Region  $\hat{R}_t$  will approximate the true high-density region  $R_\alpha$  with high-accuracy as the number of samples  $N$  and Monte Carlo iterations  $M$  goes to  $\infty$ . Similarly, for  $\mathcal{H}_{t+1}^w$ , we obtain a High-Density Region  $\hat{R}_{t+1}$ , which will

also approximate the true high-density region  $R_\alpha$  with high-accuracy. The high density regions  $\hat{R}_t = \hat{R}_{t+1} = R_\alpha$  will be equivalent as  $N, M \rightarrow \infty$ .

The definition of the Convex Hull implies uniqueness. Because of this, the Convex Hulls created from  $\hat{R}_t$  and  $\hat{R}_{t+1}$  will be the same as  $t \rightarrow \infty$ . Thus, the non-conformity score functions  $s(\cdot; \theta_t)$  and  $s(\cdot; \theta_{t+1})$  will be the same as  $t \rightarrow \infty$ .  $\square$

## D. Experiments

### D.1. Gaussian Mixture Model

This setting utilizes a Gaussian Mixture Model (GMM) with changing weights to provide intuition into the impact that changes in the non-conformity score have on the ideal miscoverage rate  $\alpha_t^*$  in settings with distribution shift. The setting involves a mixture of two normal distributions,  $\mathcal{N}_1$  and  $\mathcal{N}_2$ , mixed at time  $t$  with a weight  $w_t$ . The random variable  $z_t$  has the pdf  $p(z_t) = (1 - w_t)p(z_t|\mathcal{N}_1) + w_t p(z_t|\mathcal{N}_2)$ . The data can be seen in Figure 6. The mean and covariance of the normal distributions are:

$$\mathcal{N}_1 = \mathcal{N} \left( \begin{bmatrix} 1.0 & -1.2 \end{bmatrix}, \begin{bmatrix} 1.2 & 0.6 \\ 0.6 & 0.9 \end{bmatrix} \right); \quad \mathcal{N}_2 = \mathcal{N} \left( \begin{bmatrix} -1.0 & -1.2 \end{bmatrix}, \begin{bmatrix} 0.8 & -0.3 \\ -0.3 & 1.1 \end{bmatrix} \right)$$

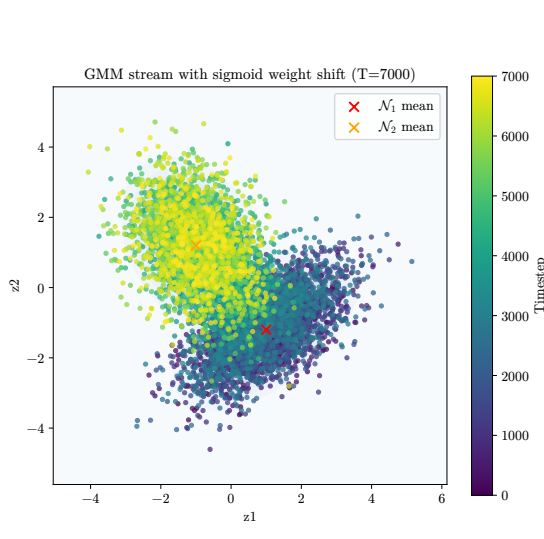


Figure 6. The 7000 points sampled from the Gaussian Mixture Model (GMM) data stream.

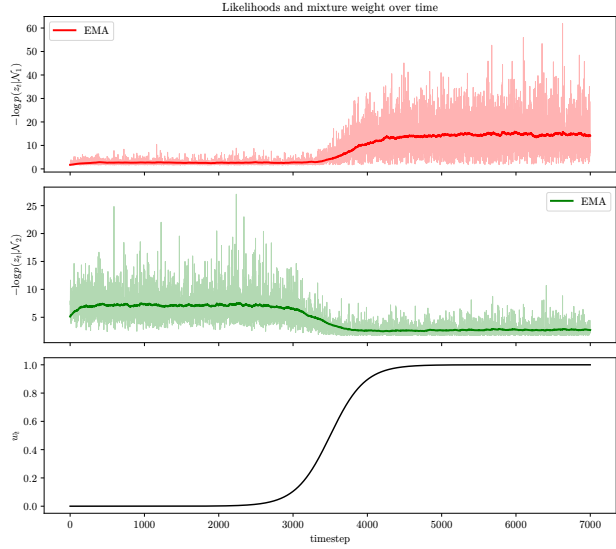
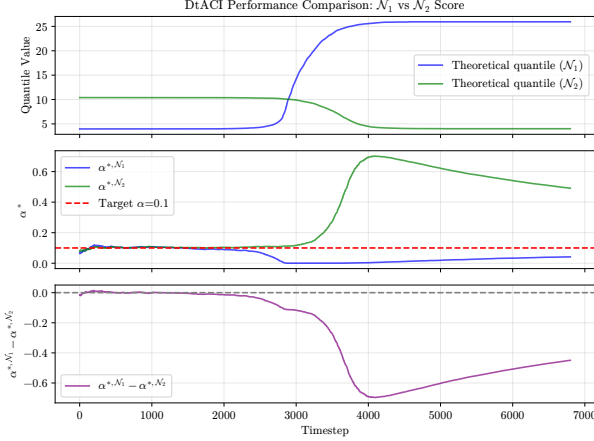


Figure 7. This figure shows the score functions evaluated as the weight parameter changes over time. We can see that the transition produces changes in the non-conformity scores.

We use the negative log-likelihood as the non-conformity score. For clarity, we define the non-conformity scores  $s_1(z) = \text{NLL}(z|\mathcal{N}_1)$ , and  $s_2(z|\mathcal{N}_2)$ . The empirical CDF  $\hat{F}_{t,\mathcal{N}_1}(s) = \frac{1}{t} \sum_{\tau=1}^t \mathbb{1}_{s_1(z_\tau) \leq s}$ , where  $z_t$  is the observation at time  $t$ . The optimal quantile is the value  $q_{1-\alpha,t}^{*,\mathcal{N}_1} = \inf_q \{q : \Pr[s_1(z_t) \leq q] \geq 1 - \alpha\}$ , which induces the optimal miscoverage rate  $\alpha_t^{*,\mathcal{N}_1} = \hat{F}_{t,\mathcal{N}_1}^{-1}(q_{1-\alpha,t}^{*,\mathcal{N}_1})$ . These quantities are similarly defined for the non-conformity score  $s_2$ . Note that the optimal quantile and the optimal miscoverage rate are only dependent on the two score functions, and do not assume that the data are drawn from these distributions. We can see the value of the non-conformity scores as the weight parameter changes in Figure 7. Based on the non-conformity scores, we can also calculate the values of our optimal  $\alpha_t^*$  under each score function.

This is shown in Figure 8. The figure depicts the difference in  $\alpha_t^*$  over time. This quantity is of interest to us, as the theoretical bound Remark 5.2 is dependent on the difference between subsequent  $\alpha_t^*$ . While the change in  $\alpha_t^{*,\mathcal{N}_1}$  and  $\alpha_t^{*,\mathcal{N}_2}$  is smooth, the problem we encounter in settings with score function change is that the difference between the two  $\alpha_t^*$  can be large. This indicates that if we were to switch score functions at the time of distribution shift, we would incur a large regret penalty, as our miscoverage rate would be poorly calibrated to the new score function. This motivates the need for adaptive miscoverage rates in settings with distribution shift and changing score functions. The counterfactual replay mechanism we propose in Section 4 is designed to mitigate this issue by replacing a potentially abrupt change in  $\alpha_t^*$  due to a score function shift, to the local evolution of  $\alpha_t^{*,\mathcal{N}_2}$ , which is much smoother.

This is evidenced in Figure 9, where we compare the local and global coverage of DtACI using fixed score functions  $s_1$  and  $s_2$ , against AdaptNC which adapts to the changing score function. We can see that when the score function is misaligned with the dominant mixture component, DtACI suffers from sharp under-coverage during the transition period, as well as persistent bias in global coverage. In contrast, AdaptNC is able to maintain near-target local and global coverage throughout



**Figure 8.** This figure shows the impact of changing nonconformity scores under a shifting GMM. **Top:** We compute the induced theoretical  $(1 - \alpha)$  quantiles for each score function, which shift in opposite directions as the dominant mixture component changes. **Middle:** The corresponding optimal miscoverage rates  $\alpha_t^*$  implied by each score function, illustrating that distribution shift can make the *ideal* miscoverage rate deviate substantially from the nominal  $\alpha = 0.1$  (red dashed), purely due to the change in score distribution. **Bottom:** The difference between the two  $\alpha_t^*$ .

the data stream, demonstrating the effectiveness of our adaptive miscoverage rate approach in handling distribution shift and changing non-conformity scores.

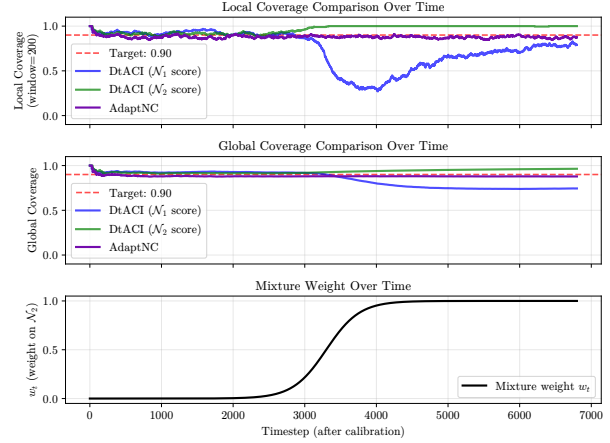


**Figure 9.** This figure shows the local and global coverage performance under a shifting GMM. We compare DtACI using the fixed score  $s_1$ , DtACI using the fixed score  $s_2$ , and AdaptNC. **Top:** Local (sliding-window) coverage with window size  $w = 200$  against the  $1 - \alpha = 0.90$  target, highlighting that a mismatched score can lead to sharp under-coverage during the transition while AdaptNC remains near-target. **Middle:** Global coverage over time, showing persistent bias for DtACI when the score is misaligned with the dominant mixture component. **Bottom:** The mixture weight  $w_t$  on  $\mathcal{N}_2$ , which induces the distribution shift driving the coverage changes.

## D.2. Indoor Localization

This section provides a complete and reproducible description of the environment dynamics, wireless observation model, trajectory predictor, and evaluation policy used in all experiments.

### D.2.1. ENVIRONMENT DYNAMICS

We consider a planar indoor localization environment with discrete-time dynamics and sampling period  $\Delta t = 0.1$  s. The true system state at time  $t$  is

$$\mathbf{s}_t = [x_t, y_t, v_{x,t}, v_{y,t}]^\top \in \mathbb{R}^4,$$

where  $(x_t, y_t)$  denotes the agent position and  $(v_{x,t}, v_{y,t})$  denotes velocity.

Given an acceleration control input  $\mathbf{a}_t = [a_{x,t}, a_{y,t}]^\top$ , the dynamics evolve according to

$$\begin{aligned} x_{t+1} &= x_t + \Delta t v_{x,t}, \\ y_{t+1} &= y_t + \Delta t v_{y,t}, \\ v_{x,t+1} &= v_{x,t} + \Delta t (a_{x,t} + \varepsilon_{x,t}), \\ v_{y,t+1} &= v_{y,t} + \Delta t (a_{y,t} + \varepsilon_{y,t}), \end{aligned}$$

where  $\varepsilon_{x,t}, \varepsilon_{y,t} \sim \mathcal{N}(0, \sigma_{\text{proc}}^2)$  model additive process noise on acceleration. We use  $\sigma_{\text{proc}} = 0.02$ .

The agent operates within a bounded workspace defined by  $x, y \in [-6, 6]$ . Reflective boundary conditions are enforced by reversing the corresponding velocity component whenever the agent reaches the workspace boundary.

### D.2.2. ACCESS POINT GEOMETRY

The environment contains four fixed access points located at

$$(-5, -5), (5, -5), (5, 5), (-5, 5).$$

These access points are static and known to the environment simulator and predictor.

### D.2.3. RSSI OBSERVATION MODEL

At each time step, the agent observes a received signal strength indicator vector

$$\mathbf{o}_t = [\text{RSSI}_t^{(1)}, \dots, \text{RSSI}_t^{(4)}]^\top \in \mathbb{R}^4.$$

Each RSSI measurement is generated as the sum of path loss, shadowing, and small-scale fading components, expressed in decibels:

$$\text{RSSI}_t^{(i)} = P_0 - 10n \log_{10}(d_t^{(i)}) + S_t^{(i)} + F_t^{(i)}.$$

**Path Loss.** The path loss component follows the standard log-distance path loss model (Rappaport, 2010). Here,  $P_0 = -30$  dB denotes the reference received power at unit distance,  $n = 2.2$  is the path loss exponent, and

$$d_t^{(i)} = \|[x_t, y_t] - \mathbf{a}_i\|_2$$

is the Euclidean distance between the agent and access point  $i$ . Distances are lower bounded by  $10^{-2}$  m to ensure numerical stability. The path loss exponent controls the rate of signal attenuation with distance and reflects indoor propagation characteristics.

**Shadowing.** Large-scale shadowing is modeled as a temporally correlated log-normal process (Gudmundson, 1991). For each access point  $i$ , the shadowing term evolves according to a first-order Gauss–Markov model:

$$S_t^{(i)} = \rho S_{t-1}^{(i)} + \sqrt{1 - \rho^2} \sigma_{\text{sh}} \xi_t^{(i)}, \quad \xi_t^{(i)} \sim \mathcal{N}(0, 1),$$

where  $\sigma_{\text{sh}} = 4.0$  dB controls the shadowing variance and  $\rho = 0.97$  determines temporal correlation. Shadowing states are initialized to zero at environment reset and evolve independently across access points.

**Small-Scale Fading.** Small-scale fading is modeled using a Rayleigh fading process generated via a sum-of-sinusoids (Jakes & Cox, 1994) method. For each access point, a complex channel coefficient  $h_t^{(i)}$  is generated, and the fading contribution is computed as

$$F_t^{(i)} = 10 \log_{10}(|h_t^{(i)}|^2 + \epsilon),$$

with  $\epsilon = 10^{-12}$  for numerical stability.

The Doppler frequency governing temporal fading correlation is velocity-dependent:

$$f_{d,t} = \frac{\|\mathbf{v}_t\|_2}{\lambda}, \quad \lambda = \frac{c}{f_c},$$

where  $f_c = 2.4$  GHz is the carrier frequency and  $c$  is the speed of light. Fading processes are independent across access points. The Rayleigh distribution of  $|h_t^{(i)}|$  follows from the assumption of rich multipath with no dominant line-of-sight component (Clarke, 1968; Rappaport, 2010).

#### D.2.4. TRAJECTORY PREDICTOR

We employ a lightweight model-based trajectory predictor that estimates the agent position from RSSI measurements using a simplified propagation model. The predictor is mismatched with the true environment observation model and does not explicitly account for shadowing or small-scale fading. This mismatch induces systematic and time-varying localization error.

**Internal State.** The predictor maintains an internal estimate of planar position and velocity,

$$\hat{\mathbf{x}}_t \in \mathbb{R}^2, \quad \hat{\mathbf{v}}_t \in \mathbb{R}^2,$$

which are reset to zero at the beginning of each rollout.

**Prediction Step.** At each time step, the predictor applies a constant-velocity motion model:

$$\hat{\mathbf{x}}_{t|t-1} = \hat{\mathbf{x}}_{t-1} + \Delta t \hat{\mathbf{v}}_{t-1}.$$

This prediction does not incorporate control inputs or process noise and serves only as a kinematic extrapolation of past estimates.

**RSSI-to-Distance Conversion.** Given an RSSI observation vector  $\mathbf{o}_t$ , the predictor converts each RSSI measurement into a distance estimate by inverting the log-distance path loss model:

$$\hat{d}_t^{(i)} = 10^{\frac{P_0 - \text{RSSI}_t^{(i)}}{10n}}.$$

This inversion assumes that RSSI measurements are generated solely by path loss and ignores the presence of shadowing and fading. As a result, the inferred distances are biased and noisy, with error statistics that depend on the instantaneous channel realization.

**Multilateration via Gauss–Newton.** The predicted position is refined by solving a nonlinear least-squares multilateration problem of the form

$$\min_{\mathbf{x} \in \mathbb{R}^2} \sum_{i=1}^N w_i \left( \|\mathbf{x} - \mathbf{a}_i\|_2 - \hat{d}_t^{(i)} \right)^2, \quad w_i = \frac{1}{(\hat{d}_t^{(i)})^2}.$$

This problem is solved using Gauss–Newton iterations initialized at  $\hat{\mathbf{x}}_{t|t-1}$ . A small damping term is added for numerical stability, and update steps are clipped to avoid large jumps. The resulting solution is denoted  $\mathbf{x}_t^{\text{meas}}$ .

**Alpha–Beta Filtering.** The final position and velocity estimates are obtained using an  $\alpha$ – $\beta$  filter:

$$\begin{aligned}\mathbf{e}_t &= \mathbf{x}_t^{\text{meas}} - \hat{\mathbf{x}}_{t|t-1}, \\ \hat{\mathbf{x}}_t &= \hat{\mathbf{x}}_{t|t-1} + \alpha \mathbf{e}_t, \\ \hat{\mathbf{v}}_t &= \hat{\mathbf{v}}_{t-1} + \frac{\beta}{\Delta t} \mathbf{e}_t,\end{aligned}$$

with  $\alpha = 0.25$  and  $\beta = 0.05$ . This filter smooths high-frequency measurement noise while allowing the predictor to track gradual motion trends.

**Model Mismatch and Error Characteristics.** Since the predictor assumes a deterministic path loss model and neglects shadowing and small-scale fading, its position estimates exhibit residual errors that are neither independent nor identically distributed. In particular, temporally correlated fading induces time-correlated localization errors whose magnitude and direction vary over time. This mismatch produces nonstationary residual streams, making the predictor suitable for evaluating adaptive conformal uncertainty estimation methods that must respond to evolving error statistics.

#### D.2.5. EVALUATION POLICY

All experiments use a fixed, non-adaptive random motion policy intended to emulate surveillance-style exploration. At each time step, acceleration inputs are sampled uniformly within bounded limits. Velocity magnitudes are clipped to a maximum of 1.0 m/s, and accelerations are bounded by 0.5 m/s<sup>2</sup>.

The policy is independent of RSSI observations, predictor estimates, and uncertainty regions. The same policy is used across all methods, ensuring that observed differences in coverage and region geometry arise solely from the uncertainty estimation method.

#### D.2.6. EXPERT WEIGHTS

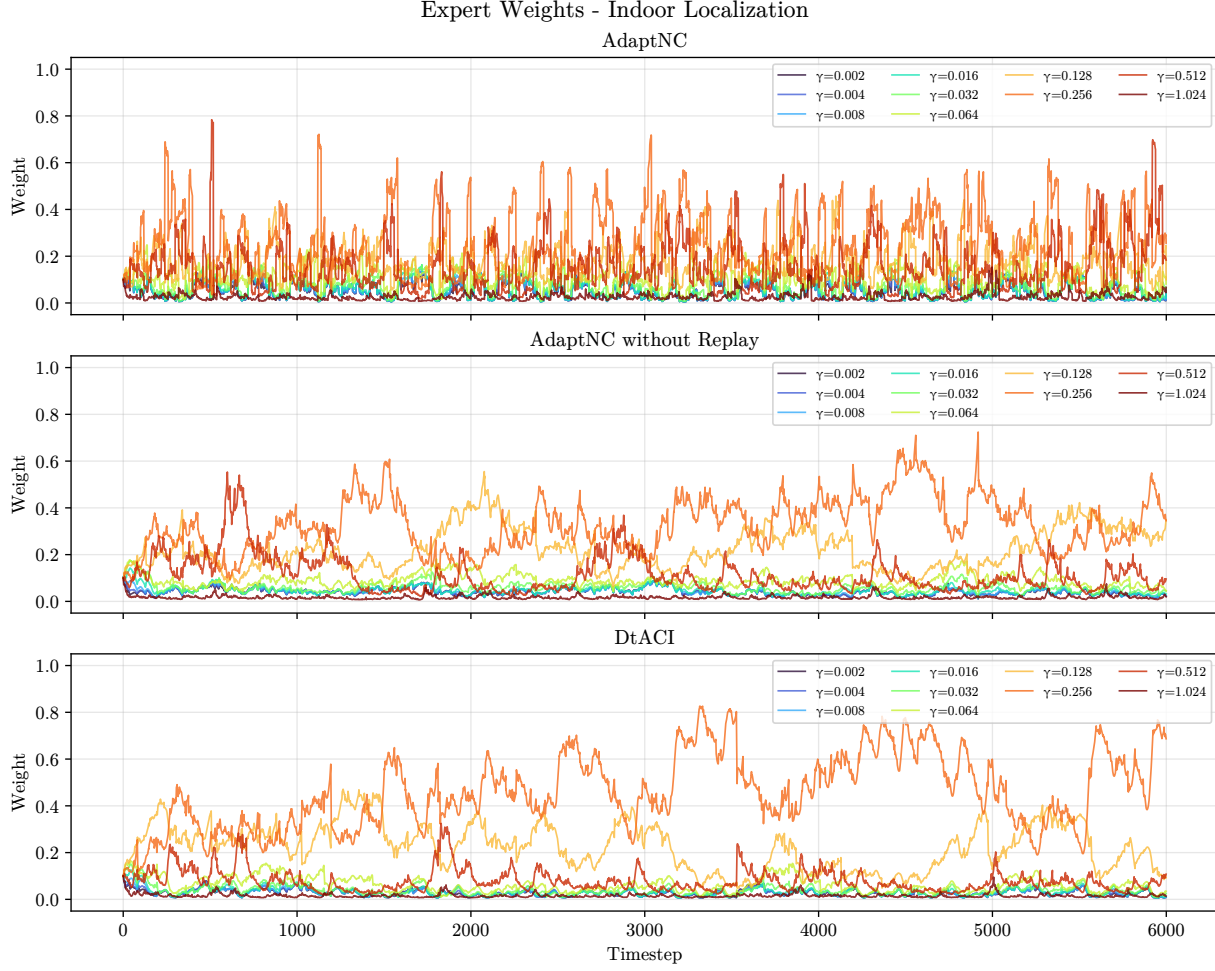


Figure 10. This figure shows the evolution of expert weights in the Indoor Localization setting over the course of the experiment. The pronounced, piecewise variation observed for AdaptNC arises from its adaptive reweighting mechanism, which enables rapid adjustment of expert weights in response to changes in the score function and contributes to maintaining valid coverage. In contrast, DtACI and AdaptNC without replay exhibit slower weight adaptation and consistently select smaller values of  $\gamma$  than AdaptNC.

### D.3. Social Navigation

The simulation environment implements a continuous-space multi-agent system based on the Social Force Model described by Helbing and Molnár (1995).

#### D.3.1. EQUATIONS OF MOTION

Let the state of agent  $\alpha$  at time  $t$  be defined by its position  $\vec{r}_\alpha(t)$ , actual velocity  $\vec{v}_\alpha(t)$ , and preferred velocity  $\vec{w}_\alpha(t)$ . The dynamics are governed by a nonlinearly dynamics equation driving the preferred velocity, subject to a maximum speed constraint.

The evolution of the preferred velocity  $\vec{w}_\alpha$  is given by:

$$\frac{d\vec{w}_\alpha}{dt} = \frac{\vec{v}_\alpha^{des} - \vec{v}_\alpha}{\tau} + \sum_{\beta \neq \alpha} \vec{F}_{\alpha\beta} + \sum_B \vec{F}_{\alpha B} + \vec{\xi}(t) \quad (23)$$

where:

- $\tau$  is the relaxation time constant.
- $\vec{v}_\alpha^{des}$  is the desired velocity vector toward the current goal.
- $\vec{F}_{\alpha\beta}$  represents the social repulsive force from agent  $\beta$ .
- $\vec{F}_{\alpha B}$  represents the repulsive force from boundary  $B$ .
- $\vec{\xi}(t)$  is a stochastic fluctuation term (Gaussian noise).

The actual velocity  $\vec{v}_\alpha(t)$  is derived by clipping the preferred velocity to the agent's maximum speed  $v_\alpha^{max}$ :

$$\vec{v}_\alpha(t) = \min \left( 1, \frac{v_\alpha^{max}}{\|\vec{w}_\alpha(t)\|} \right) \vec{w}_\alpha(t) \quad (24)$$

#### D.3.2. FORCE COMPONENTS

**Goal Attraction** The driving term attracts the agent toward its goal  $\vec{g}_\alpha$  with a desired speed  $v_\alpha^0$ :

$$\vec{v}_\alpha^{des} = v_\alpha^0 \frac{\vec{g}_\alpha - \vec{r}_\alpha}{\|\vec{g}_\alpha - \vec{r}_\alpha\|} \quad (25)$$

**Social Repulsion** The interaction force  $\vec{F}_{\alpha\beta}$  models the repulsion between agents to maintain personal space. The implementation utilizes an elliptical distance metric approximation. The force is defined as:

$$\vec{F}_{\alpha\beta} = w(\vec{e}_\alpha, \vec{f}_{\alpha\beta}) \cdot \vec{f}_{\alpha\beta} \quad (26)$$

where the raw isotropic force  $\vec{f}_{\alpha\beta}$  is:

$$\vec{f}_{\alpha\beta} = \left( \frac{A}{B} \exp \left( -\frac{b}{B} \right) \frac{2d_{\alpha\beta} - s_{ab}}{2b} \right) \vec{n}_{\alpha\beta} \quad (27)$$

with terms defined as follows:

$$\begin{aligned} d_{\alpha\beta} &= \|\vec{r}_\alpha - \vec{r}_\beta\| \quad (\text{Euclidean distance}) \\ \vec{n}_{\alpha\beta} &= \frac{\vec{r}_\alpha - \vec{r}_\beta}{d_{\alpha\beta}} \quad (\text{Normalized direction vector}) \\ s_{ab} &= \|\vec{v}_\beta\| \Delta t_{anticipation} \quad (\text{Anticipated displacement}) \end{aligned}$$

The semi-minor axis  $b$  of the repulsive potential is approximated in the implementation as:

$$b = \sqrt{\frac{d_{\alpha\beta}^2 + (d_{\alpha\beta} - s_{ab})^2}{2}} \quad (28)$$

This differs slightly from the exact equipotential formulation in the original work but preserves the qualitative elliptical avoidance behavior.

**Boundary Repulsion** Repulsion from static boundaries (walls) decays exponentially with the distance  $d_{\alpha B}$  to the nearest point on the boundary:

$$\vec{F}_{\alpha B} = w(\vec{e}_\alpha, \vec{f}_{\alpha B}) \cdot \frac{A_{wall}}{R_{wall}} \exp\left(-\frac{d_{\alpha B}}{R_{wall}}\right) \vec{n}_{\alpha B} \quad (29)$$

where  $\vec{n}_{\alpha B}$  is the normal vector pointing away from the boundary.

### D.3.3. ANISOTROPIC PERCEPTION

To reflect the limited field of view, forces are scaled by an anisotropic weight  $w(\vec{e}, \vec{f})$  dependent on the angle  $\phi$  between the agent's desired direction  $\vec{e}_\alpha$  and the force vector  $\vec{f}$ :

$$w(\vec{e}_\alpha, \vec{f}) = \begin{cases} \lambda + (1 - \lambda) \frac{1 + \cos \phi}{2} & \text{if } \cos \phi \geq 0 \quad (\text{Frontal}) \\ c & \text{if } \cos \phi < 0 \quad (\text{Rear}) \end{cases} \quad (30)$$

where  $\cos \phi = \frac{\vec{e}_\alpha \cdot \vec{f}}{\|\vec{e}_\alpha\| \|\vec{f}\|}$ .

### D.3.4. MODEL PARAMETERS

The default parameters used in the simulation are listed in Table 3.

Parameter	Symbol	Value
Relaxation time	$\tau$	0.5 s
Desired speed	$v^0$	$\mathcal{N}(1.34, 0.26)$ m/s
Max speed	$v^{max}$	$1.3 \times v^0$ m/s
Repulsion strength	$A$	5.0 m/s <sup>2</sup>
Repulsion range	$B$	2.0 m
Anticipation time	$\Delta t_{anticipation}$	2.0 s
Anisotropy factor	$\lambda$	0.5
Rear influence	$c$	0.5
Wall repulsion strength	$A_{wall}$	10.0 m/s <sup>2</sup>
Wall repulsion range	$R_{wall}$	0.2 m

Table 3. Simulation parameters corresponding to the Social Navigation experiment

### D.3.5. TRAJECTORY PREDICTOR

The trajectory predictor is implemented as an Long Short-Term Memory (LSTM) to capture temporal dependencies in agent motion. The model is implemented using the Flax/JAX framework.

**Architecture** The model processes a sequence of state observations  $X = \{x_1, \dots, x_T\}$  where each timestep  $x_t \in \mathbb{R}^{34}$  contains the ego-agent's state and the relative states of the  $k = 7$  nearest neighbors. The specific feature composition is:

- **Ego Features (6):** Absolute position  $(p_x, p_y)$ , velocity  $(v_x, v_y)$ , and goal position  $(g_x, g_y)$ .
- **Neighbor Features (28):** Relative position  $(\Delta p_x, \Delta p_y)$  and relative velocity  $(\Delta v_x, \Delta v_y)$  for each of the 7 nearest neighbors.

The network architecture consists of a single LSTM layer with a hidden dimension of  $h = 128$ . The final hidden state  $h_T$  is passed through a Multi-Layer Perceptron (MLP) head to predict the 2D position  $\hat{y} \in \mathbb{R}^2$  of the agent at the prediction horizon  $\tau$ :

$$h_{1:T} = \text{LSTM}(x_{1:T}) \quad (31)$$

$$z = \text{ReLU}(\text{Dense}_{128}(\text{Dropout}(h_T))) \quad (32)$$

$$\hat{y} = \text{Dense}_2(\text{Dropout}(z)) \quad (33)$$

Dropout with a rate of 0.1 is applied before the dense layers during training to prevent overfitting.

**Training Objective** The model is trained to minimize the Mean Squared Error (MSE) between the predicted position  $\hat{y}$  and the ground truth position  $y$  after  $\tau$  simulation steps:

$$\mathcal{L}(\theta) = \frac{1}{N} \sum_{i=1}^N \|\hat{y}_i - y_i\|^2 \quad (34)$$

Optimization is performed using the AdamW optimizer. The specific hyperparameters used for training are detailed in Table 4.

Hyperparameter	Value
Hidden Dimension	128
Dropout Rate	0.1
Sequence Length ( $T$ )	10
Prediction Horizon ( $\tau$ )	5
Learning Rate	$1 \times 10^{-4}$
Weight Decay	$1 \times 10^{-5}$
Batch Size	512
Training Epochs	200

Table 4. Hyperparameters for the LSTM Trajectory Predictor.

#### D.3.6. EXPERT WEIGHTS



Figure 11. This figure contains the expert weights for the social navigation setting. The plots show the evolution of the weights over the course of the scenario. The staccato pattern of the AdaptNC setting is a consequence of the adaptive reweighting scheme, which enables rapid adaptation of the expert weights in response to score function changes, which helps AdaptNC maintain coverage. We can see that the DtACI and AdaptNC without Replay methods do not adapt expert weights as quickly, and choose values for  $\gamma$  that are lower than those chosen by AdaptNC.

## D.4. Multirotor Tracking

This section describes the multirotor environment with actuator degradation, the trajectory predictor used for position forecasting, and the control policy employed to generate training, calibration, and evaluation trajectories.

### D.4.1. ENVIRONMENT WITH ACTUATOR DEGRADATION

The multirotor state at time  $t$  is

$$\mathbf{s}_t = [x_t, \dot{x}_t, y_t, \dot{y}_t, z_t, \dot{z}_t, \psi_t, \dot{\psi}_t, \theta_t, \dot{\theta}_t, \delta_t, \dot{\delta}_t]^\top \in \mathbb{R}^{12},$$

where  $(x, y, z)$  denote position,  $(\dot{x}, \dot{y}, \dot{z})$  translational velocity,  $\psi$  yaw,  $\theta$  pitch, and  $\delta$  roll.

The system evolves in discrete time with integration step  $\Delta t = 0.1$  s using forward Euler integration.

**Control Inputs.** The control input is

$$\mathbf{u}_t = [u_{1,t}, u_{2,t}, u_{3,t}, u_{4,t}]^\top,$$

where  $u_1$  corresponds to collective thrust,  $u_2$  to pitch torque,  $u_3$  to roll torque, and  $u_4$  to yaw torque.

**Actuator Degradation.** Each actuator is subject to stochastic degradation modeled by a health variable

$$\boldsymbol{\Gamma}_t \in [0, 1]^4,$$

where  $\Gamma_t^{(i)} = 1$  denotes a healthy actuator. The effective control applied to the system is

$$\mathbf{u}_t^{\text{eff}} = \boldsymbol{\Gamma}_t \odot \mathbf{u}_t.$$

Actuator health evolves according to an additive Wiener process with negative drift:

$$\boldsymbol{\Gamma}_{t+1} = \boldsymbol{\Gamma}_t - \alpha \Delta t + \sigma \mathbf{w}_t, \quad \mathbf{w}_t \sim \mathcal{N}(\mathbf{0}, \Delta t I),$$

with  $\alpha = 5 \times 10^{-4}$  and  $\sigma = 2.5 \times 10^{-4}$ . The degradation process is unobserved by the predictor and policy.

**Dynamics.** Translational accelerations are given by

$$\ddot{x}_t = g\theta_t, \quad \ddot{y}_t = -g\delta_t, \quad \ddot{z}_t = u_{1,t}^{\text{eff}} - g,$$

with gravitational constant  $g = 9.81$  m/s<sup>2</sup>. Rotational accelerations satisfy

$$\ddot{\psi}_t = u_{4,t}^{\text{eff}}, \quad \ddot{\theta}_t = u_{2,t}^{\text{eff}}, \quad \ddot{\delta}_t = u_{3,t}^{\text{eff}}.$$

Yaw is wrapped to  $[-\pi, \pi]$ , and pitch and roll are clipped to  $[-0.3, 0.3]$  radians.

### D.4.2. TRAJECTORY PREDICTOR

To forecast planar motion, we use a hybrid physics learning predictor that combines a simple kinematic prior with a learned residual model.

**Physics Prior.** The prior assumes constant velocity motion in the horizontal plane:

$$\hat{x}_{t+1}^{\text{phys}} = x_t + \Delta t \dot{x}_t, \quad \hat{y}_{t+1}^{\text{phys}} = y_t + \Delta t \dot{y}_t.$$

This prior ignores rotational coupling and actuator degradation and therefore provides only a coarse approximation of the true dynamics.

**Residual Learning.** Rather than predicting absolute positions, the predictor learns the residual

$$\mathbf{r}_t = \begin{bmatrix} x_{t+1} \\ y_{t+1} \end{bmatrix} - \begin{bmatrix} \hat{x}_{t+1}^{\text{phys}} \\ \hat{y}_{t+1}^{\text{phys}} \end{bmatrix}.$$

The final prediction is obtained as

$$\hat{\mathbf{p}}_{t+1} = \begin{bmatrix} \hat{x}_{t+1}^{\text{phys}} \\ \hat{y}_{t+1}^{\text{phys}} \end{bmatrix} + \hat{\mathbf{r}}_t.$$

**LSTM Architecture and Training.** Residuals are predicted using a single layer long short term memory network that takes as input a fixed length history

$$[\mathbf{s}_{t-H+1}, \dots, \mathbf{s}_t] \in \mathbb{R}^{H \times 12},$$

with  $H = 50$ . The LSTM hidden dimension is 128, and the output is a two dimensional residual  $(r_x, r_y)$ . The network is trained by minimizing mean squared error between predicted and true residuals using supervised data generated from the environment.

**Model Mismatch.** The predictor does not observe actuator health and does not model degradation dynamics. As actuator effectiveness degrades over time, the physics prior becomes increasingly inaccurate. Although the LSTM can partially compensate using temporal context, prediction errors remain time varying and correlated, providing a nonstationary residual process.

#### D.4.3. EVALUATION POLICY

All trajectories are generated using a fixed model predictive path integral control policy. The policy is used solely to excite the system and is not part of the proposed uncertainty estimation method.

**Reference Motion.** The policy tracks a figure eight trajectory in the horizontal plane:

$$x_r(t) = A \sin(\omega t), \quad y_r(t) = A \sin(2\omega t),$$

with amplitude  $A = 3.0$  and angular frequency  $\omega = 0.25$ . A constant altitude reference  $z_r = 2.0$  m is enforced using a proportional derivative controller on thrust.

**MPPI Control.** At each time step, the policy samples  $N = 30$  control sequences over a horizon of  $H = 35$  by perturbing a nominal sequence with Gaussian noise. Each sequence is rolled out using the environment dynamics, and a quadratic cost penalizing position tracking error, velocity error, attitude deviation, and control effort is accumulated. Sampled trajectories are weighted using an exponential transformation of cost, and the nominal sequence is updated accordingly. The first control input is applied, and the horizon is receded.

**Policy Independence.** The policy does not observe actuator health, predictor outputs, or uncertainty regions. The same policy and parameters are used across all experiments. Consequently, differences in coverage and region geometry arise solely from the uncertainty estimation method rather than from changes in control behavior.

#### D.4.4. EXPERT WEIGHTS

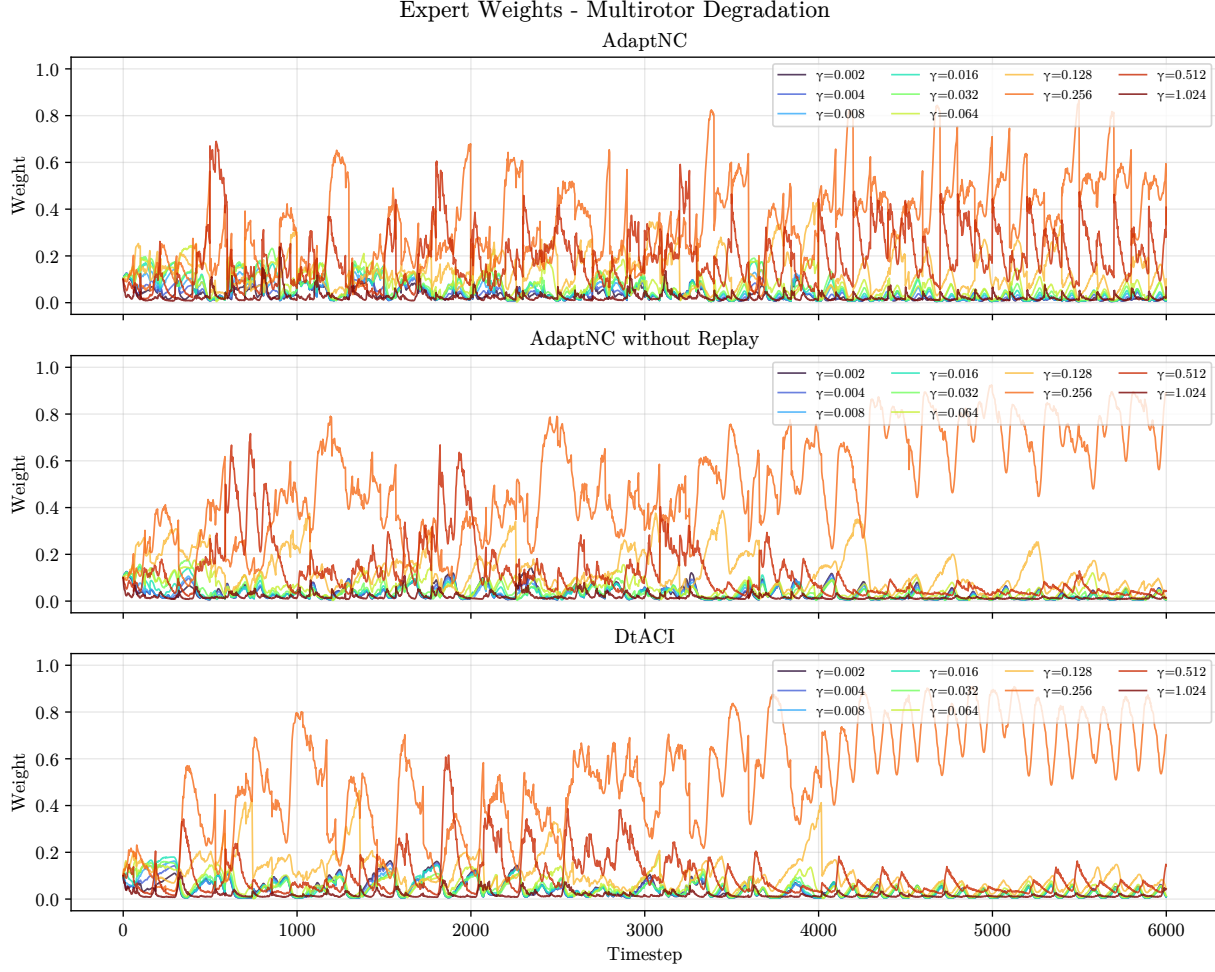


Figure 12. This figure shows the evolution of expert weights in the multirotor navigation setting. The plots illustrate how weights change over time across the different methods. The pronounced oscillatory pattern observed for AdaptNC arises from its adaptive reweighting mechanism, which enables rapid adjustment of expert weights in response to changes in the nonconformity score and contributes to maintaining coverage. In contrast, DtACI and AdaptNC without Replay exhibit slower weight adaptation and assign greater weight to intermediate values of  $\gamma$  toward the end of the rollout, resulting in reduced responsiveness compared to AdaptNC.